

1 **Phosphatidylserine Receptors Enhance SARS-CoV-2 Infection: AXL as a Therapeutic
2 Target for COVID-19**

3

4

5 Dana Bohan^{1*}, Hanora Van Ert^{1*}, Natalie Ruggio¹, Kai J. Rogers¹, Mohammad Badreddine¹,
6 José A. Aguilar Briseño¹, Robert Anthony Rojas Chavez¹, Boning Gao², Tomasz Stokowy³,
7 Eleni Christakou^{3, 4}, David Micklem⁴, Gro Gausdal⁴, Hillel Haim¹, John Minna², James B. Lorens³
8 and Wendy Maury^{1†}

9

10 ¹ Department of Microbiology and Immunology, University of Iowa, Iowa City, IA

11 ² Hamon Center for Therapeutic Oncology Research, University of Texas Southwestern Medical
12 Center, Dallas, TX

13 ³ Department of Biomedicine, University of Bergen, Bergen Norway.

14 ⁴ BerGenBio ASA, Bergen, Norway.

15 * These authors contributed equally to this work.

16 † Corresponding author

17

18 **Short Title:** Phosphatidylserine Receptors Enhance SARS-CoV-2 Entry

19 **Keywords:** SARS-CoV-2, COVID19, phosphatidylserine receptor, apoptotic mimicry, viral entry,
20 AXL, bemcentinib, TIM-1, ACE2, TMPRSS2

21 **Author summary word count:** 191

22 **Total character count (including spaces, excluding STAR Methods and supplemental
23 figure legends):** 41,935

24 **AUTHOR SUMMARY**

25 Phosphatidylserine (PS) receptors are PS binding proteins that mediate uptake of apoptotic
26 bodies. Many enveloped viruses utilize this PS/PS receptor mechanism to adhere to and
27 internalize into the endosomal compartment of cells and this is termed apoptotic mimicry. For
28 viruses that have a mechanism(s) of endosomal escape, apoptotic mimicry is a productive route
29 of virus entry. We evaluated if PS receptors serve as cell surface receptors for SARS-CoV-2
30 and found that the PS receptors, AXL, TIM-1 and TIM-4, facilitated virus infection when low
31 concentrations of the SARS-CoV-2 cognate receptor, ACE2, was present. Consistent with the
32 established mechanism of PS receptor utilization by other viruses, PS liposomes competed with
33 SARS-CoV-2 for binding and entry. We demonstrated that this PS receptor enhances SARS-
34 CoV-2 binding to and infection of an array of human lung cell lines and is an under-appreciated
35 but potentially important host factor facilitating SARS-CoV-2 entry.

36

37

38 **INTRODUCTION**

39 Severe Acute Respiratory Syndrome Coronavirus 2 (SARS-CoV-2) emerged in late 2019 and
40 quickly spread around the world, resulting in the current public health pandemic. SARS-CoV-2 is
41 a beta coronavirus of the sarbecovirus subgenus and is closely related to SARS-CoV, the agent
42 responsible for an epidemic in 2003. SARS-CoV-2 is effectively transmitted between humans
43 and has infected more than 178 million individuals and caused more than 3.88 million deaths
44 worldwide as of June 23, 2021 (WHO). Fortunately, a herculean scientific effort has resulted in
45 the development of SARS-CoV-2 vaccines which have been shown to be efficacious, potentially
46 stemming the pandemic. Nonetheless, in combination with vaccines, continued development of
47 efficacious antivirals is needed, as outbreaks continue in under-vaccinated regions and severe
48 disease is not eradicated following vaccination. Towards this goal, a more comprehensive
49 understanding of SARS-CoV-2 interactions with host cells will be required.

50

51 SARS-CoV-2 entry into cells is mediated by the viral spike glycoprotein (S) binding to
52 Angiotensin Converting Enzyme 2 (ACE2) (1-3). The S1 subunit of S binds to ACE2 while S2
53 mediates membrane fusion. Cleavage at the S1/S2 junction occurs during virus egress from
54 producer cells by the host protease furin which facilitates S1 binding to ACE2. A second site
55 termed S2' is also cleaved by the host proteases. Cleavage by TMPRSS2 at the cell surface
56 promotes fusion of the viral and host plasma membranes (2, 4). Alternatively, SARS-CoV-2
57 virions can be internalized via clathrin-mediated endocytosis after ACE2 binding, wherein host

58 cathepsins (especially cathepsin L) proteolytically cleave S2' (3, 5-7). Adherence factors that
59 enhance virion binding and increase infectivity have also been identified, namely neuropilin 1
60 and heparan sulfate (8, 9).

61

62 Binding and internalization of a variety of different enveloped viruses occurs through virion
63 associated phosphatidylserine (PS) binding to PS receptors. Members of the TIM family (TIM-1
64 and TIM-4) bind PS directly while another family of PS receptors, the TAM tyrosine kinase
65 receptor family (TYRO3, AXL and MERTK), bind PS indirectly through the adaptor proteins
66 Gas6 and Protein S. These PS receptor mediate binding and internalization of a wide range of
67 viruses, including filoviruses, alphaviruses, and flaviviruses (10-13). TIM-1, TIM-4, and AXL
68 appear to be the most efficacious at mediating viral entry given their prevalent use among
69 enveloped viruses (14-16). Once virions are within the endosome, events that result in virion
70 fusion with cellular membranes are virus specific, with filoviruses requiring viral glycoprotein
71 processing followed by interactions with Niemann Pick C1 protein (NPC1) to initiate fusion,
72 whereas flaviviruses rely on endosomal acidification driving glycoprotein conformational
73 changes which mediate fusion (17, 18).

74

75 Given that PS receptors mediate entry of other enveloped viruses through interactions with viral
76 membrane PS, we assessed the role of PS receptors on SARS-CoV-2 infection and the
77 mechanism of interaction. We found that plasma membrane-expressed PS receptors by
78 themselves do not result in productive SARS-CoV-2 infection; however, these receptors
79 enhance infection when low levels of ACE2 are expressed. Our findings indicate that these
80 receptors synergize with ACE2 to mediate SARS-CoV-2 entry through PS-dependent
81 interactions. These data are in contrast to the conclusions drawn by another report stating that
82 AXL interacts directly with the SARS-CoV-2 spike protein (19). Appreciation of this route of entry
83 provides an additional pathway that could be therapeutically targeted to inhibit virus entry and
84 subsequent infection.

85

86

87 **RESULTS**

88 ***PS receptors enhance ACE2-dependent SARS-CoV-2 infection***

89 The ability of TIM and TAM family PS receptors to support SARS-CoV-2 infection were initially
90 examined in transfected HEK 293T cells. Wild-type HEK 293T cells do not express significant
91 amounts of ACE2 or PS receptors and are poorly permissive to SARS-CoV-2 infection (3, 20).

92 Expression plasmids encoding ACE2 and/or the PS receptors, AXL or TIM-1, were transfected,
93 resulting in expression of these receptors on the surface of the transfected cells (**S1A-B**). Dual
94 transfection did not alter expression of ACE2 or PS receptors relative to single transfection. The
95 PS receptors AXL and TIM-1 by themselves did not facilitate infection of SARS-CoV-2 or VSV
96 pseudovirions bearing SARS-CoV-2 spike (VSV/Spike) (**Fig. 1A, S1C**). However, when low
97 levels of ACE2 (50 to 250 ng of plasmid) were co-expressed with either AXL or TIM-1, the
98 combinations enhanced infection over that observed with ACE2 alone. TIM-1-enhanced ACE2-
99 dependent recombinant VSV/Spike (rVSV/Spike) (21) infection, and enhancement occurred
100 over a wider range of ACE2 concentrations than AXL-enhanced ACE2-dependent infection, with
101 AXL consistently enhancing infection when 250 ng of ACE2 plasmid was transfected (**Fig. 1B-**
102 **C, S1C**). The more limited ability of AXL to synergize was not due to limiting Gas6 in the media
103 as the addition of Gas6 to media did not enhance the synergy. At higher concentrations of
104 ACE2 plasmid, PS receptor enhancement of infectivity was reduced and, with transfection of 1
105 µg of ACE2 plasmid, no PS receptor enhancement was observed. Thus, only when ACE2 is
106 limiting on the cell surface do PS receptors facilitate infection. Consistent with a role for PS
107 receptors in SARS-CoV-2 entry, we observed enhanced virion attachment to cells when PS
108 receptors were expressed (**Fig. 1D**). In addition to viral load assessments, supernatants from
109 SARS-CoV-2 infected HEK 293T cultures were evaluated for production of infectious virions at
110 48 hpi by TCID₅₀ assays in Vero E6 cells that express TMPRSS2. Low levels (50 ng) of ACE2
111 transfection increased virion production and this was enhanced by co-expression of TIM-1 (**Fig.**
112 **1E**). Consistent with the viral load findings, AXL co-expression was not effective at enhancing
113 production of infectious virus when this low level of AXL was transfected. Other PS receptors,
114 TIM-4, TYRO3, and MerTK were examined for their ability of enhance infection. TIM-4
115 enhanced ACE2-dependent entry of VSV/Spike in a manner similar to TIM-1; however, TYRO3
116 and MerTK of the TAM family did not mediate increased entry, despite detectable levels of
117 plasma membrane expression after transfection (**Fig. 1F; S1A-B; S1D**). The synergy between
118 PS receptors and ACE2 was specific for SARS-CoV-2 as infection with VSV-luciferase
119 pseudovirions bearing Lassa virus GP was not affected by expression of these receptors (**S1E**).
120 These studies indicate that PS receptors synergize with low levels of ACE2 to enhance SARS-
121 CoV-2 infection. Further, these data provide evidence that VSV/Spike pseudovirions serve as a
122 useful BSL2 surrogate for SARS-CoV-2 entry events as others have shown (22-24).
123

124 **PS receptors bind to virion associated PS, not the SARS-CoV-2 Spike protein**

125 We took several different approaches to examine the mechanism by which PS receptors
126 interact with SARS-CoV-2. In the context of other viral pathogens, PS receptors are known to
127 bind to virion membrane associated PS and mediate endosomal internalization of virions,
128 shuttling virus to cognate endosomal receptors. Liposomes composed of PS compete for virion
129 binding to PS receptors (25). To test this with SARS-CoV-2, increasing concentrations of PS or
130 phosphatidylcholine (PC) liposomes were evaluated for their ability to compete with virus for PS
131 binding sites in ACE2 + AXL or ACE2 + TIM-1 transfected HEK 293T cells. PS liposomes
132 effectively blocked VSV/Spike entry, whereas PC liposomes were significantly less effective
133 (**Fig. 2A-B**). We also assessed the activity of a TIM-1 mutant, ND115DN which has a disrupted
134 TIM-1 PS binding pocket, for its ability to facilitate VSV/Spike entry. This TIM-1 mutant did not
135 synergize with ACE2, indicating that the TIM-1 PS binding pocket is critical for this enhanced
136 activity (**Fig. 2C**) (12, 20).

137
138 Others have reported that the N-terminal domain of SARS-CoV-2 spike directly binds to AXL
139 and is important for AXL-mediated entry of SARS-CoV-2 (19). To assess spike/AXL
140 interactions, purified soluble full-length SARS-CoV-2 spike-Fc, spike receptor binding domain-
141 Fc (RBD) or spike N-terminal domain-Fc (NTD) was incubated with HEK 293T cells transiently
142 expressing AXL. Flow cytometry was used to detect spike proteins bound to AXL. Parallel ACE2
143 binding to soluble SARS-CoV-2 spike served as a positive control. As the spike NTD-Fc was
144 not expected to bind to ACE2, an ELISA confirmed the ability of a conformationally dependent
145 α -spike NTD monoclonal antibody to bind NTD-Fc, suggesting that NTD-Fc was in its native
146 conformation (**S2B**). The full-length spike-Fc and the RBD-Fc bound to ACE2, but no
147 interactions were detected between any of the purified spike proteins and AXL (**Fig. 2D**) despite
148 evidence of robust AXL surface expression on transfected HEK 293T cells (**S2A**) and the
149 equivalent levels of detection of the purified proteins via ELISAs (**S2C**). Biolayer interferometry
150 studies confirmed and extended our findings that recombinant AXL does not bind to purified
151 NTD, whereas interaction with the α -spike NTD monoclonal antibody was readily detected (**Fig.**
152 **2E**). Thus, using two complementary approaches, we were unable to demonstrate direct
153 interactions of AXL with spike. In total, our studies are consistent with PS receptors interacting
154 with SARS-CoV-2 virions through the well-established mechanism of virion-associated PS
155 binding to TIM-1 and AXL.

156

157 **Redundant routes of virus entry: endosomal vs. plasma membrane mediated infection**

158 ACE2-dependent coronaviruses enter cells through two different routes: 1) An endosomal route
159 of virus uptake that requires low pH-dependent cathepsin L processing of spike, and 2) A
160 plasma membrane route that is dependent upon TMPRSS2 cleavage of spike (3, 26). Others
161 have reported that TMPRSS2-dependent entry is preferentially utilized by the virus when this
162 serine protease is expressed (27). We examined the route of virus entry at play when ACE2, PS
163 receptors and/or TMPRSS2 was expressed.

164

165 Initially, we assessed enhancement conferred by increasing amounts of TMPRSS2 plasmid on
166 ACE2-dependent infection. As anticipated, we found that low levels (10 ng) of TMPRSS2
167 expressing plasmid enhanced VSV/Spike pseudovirion entry in HEK 293T cells co-transfected
168 with 50 ng of ACE2 expressing plasmid (**Fig. 3A**). However, at higher concentrations of
169 TMPRSS2 plasmid, TMPRSS2 did not enhance infection, perhaps due to aberrant protease
170 activity. Inverting these variables, when 10 ng of TMPRSS2 plasmid was transfected in the
171 presence of low concentrations of ACE2, TMPRSS2 enhanced virus infection (**Fig. 3B**). At high
172 concentrations of ACE2, virus entry became TMPRSS2-independent in a manner similar to the
173 effects of the PS receptors. Taken with Fig. 1B and C, these studies indicate that the PS
174 receptors and TMPRSS2 can facilitate ACE2-dependent virus infection when ACE2 is limiting,
175 but with increasing ACE2 concentrations the infections become independent of these entry
176 factors. This may be related to effects of soluble ACE2 on entry (28).

177

178 To evaluate how PS receptors and/or TMPRSS2 expression would alter the route of ACE2-
179 dependent infection, HEK 293T cells were transfected PS receptors as before and infected with
180 VSV/Spike in the presence or absence of the cysteine protease inhibitor, E-64, that blocks
181 endosomal cathepsin activity. Non-toxic levels of E-64 were effective at blocking ACE2-
182 dependent infection (**Fig. 3C, S3**), indicating that virions were entering these cells in a cysteine
183 protease-dependent manner, likely through the endosomal compartment. The enhancement of
184 virus entry conferred by the combination of PS receptors and ACE2 was also inhibited by E-64,
185 providing evidence that this is the route of virion uptake that is enhanced by PS receptors.
186 These findings are consistent with earlier reports that PS receptors mediate cargo
187 internalization into the endosomal compartment (12, 13, 29). In cells that expressed ACE2 and
188 TMPRSS2, virus entry was no longer sensitive to E-64 as previously reported (6, 27).
189 VSV/Spike entry in the presence of TMPRSS2, PS receptors, and ACE2, was also insensitive to
190 E-64, suggesting that the TMPRSS2 expression and activity mediates entry at the plasma
191 membrane independent of PS receptor utilization.

192

193 ***Inhibition of endogenous AXL utilization blocks SARS-CoV-2 entry***

194 We next evaluated the ability of endogenously expressed PS receptors to enhance SARS-CoV-
195 2 in ACE2 positive cells. Vero E6 cells that express ACE2, AXL, and TIM-1 (**S4A**) were initially
196 assessed (20). Notably, a large fraction of ACE2 protein is located intracellularly, suggesting a
197 rich reserve of ACE2 is inaccessible to extracellular virions (**S4B**). Initial studies using PS
198 liposomes confirmed that PS receptors are important for SARS-CoV-2 infection of these cells.
199 Competition studies in Vero E6 cells demonstrated that increasing doses of PS, but not PC,
200 inhibited VSV/Spike infection, similar to our findings in HEK 293T cells (**Fig. 4A**). PS liposomes
201 also significantly reduced SARS-CoV-2 binding to the surface of Vero E6 cells, implicating PS
202 receptors in attachment and subsequent entry of SARS-CoV-2 (**Fig. 4B**). These findings
203 reinforce the importance of either AXL, TIM-1, or both for SARS-CoV-2 entry.

204

205 To assess if AXL was important for infection of Vero E6 cells, the selective AXL kinase inhibitor,
206 bermcentinib, was tested for its ability to block SARS-CoV-2 infection. In a dose dependent
207 manner, bermcentinib profoundly inhibited SARS-CoV-2 virus load and blocked infection of the
208 one-hit VSV/Spike pseudovirion (**Fig. 4C, S4D**). A time-of-addition study indicated that
209 bermcentinib inhibition was most effective at early timepoints during SARS-CoV-2 infection,
210 consistent with a role of AXL in virus entry (**Fig. 4D**). Bemcentinib toxicity was tested on human
211 lung epithelial cells and was nontoxic at the concentrations used (**S4C**). Consistent with an
212 important role for AXL in SARS-CoV-2 infection, RNAseq of infected Vero E6 demonstrated that
213 infection of these cells with a MOI of 0.01 resulted in ~80% of transcripts composed of viral
214 transcripts 18 hpi (**Fig. 4E**). If these cells were treated with 1 μ M bermcentinib at the time of
215 infection, the fraction of viral transcripts dropped precipitously, decreasing to ~10% of the total
216 reads.

217

218 To determine if TIM-1 contributed to SARS-CoV-2 infection of Vero E6 cells, the blocking anti-
219 human TIM-1 monoclonal antibody, ARD5, was evaluated for inhibition of recombinant VSV
220 (rVSV) bearing either Ebola GP (EBOV) or spike. While rVSV/EBOV GP was inhibited by ARD5
221 as previously reported (12, 30), it had no effect on rVSV/Spike infection (**S4E**). Thus, despite
222 robust expression of both PS receptors, AXL is preferentially utilized for SARS-CoV-2 infection
223 in these cells. While preferential PS receptor utilization has been reported for other pathogens
224 (20), our previous studies indicated that TIM-1 rather than AXL was preferentially used, in
225 contrast to our current observations with SARS-CoV-2. Host factors or virion attributes

226 determining PS receptor preference are currently unexplored. A broad-spectrum TAM inhibitor,
227 BMS777607, modestly reduced virus infection in a dose dependent manner (**Fig. 4F**),
228 discounting the likelihood of off-target effects with bemcentinib.

229

230 As the bulk of ACE2 in Vero E6 cells is intracellular (**S4B**), surface expressed-AXL may be
231 facilitating SARS-CoV-2 uptake into the endosomal compartment where proteolytic processing
232 and ACE2 interactions mediate fusion of the viral envelope and cellular membranes. Previous
233 studies with the betacoronavirus responsible for the 2003-2004 outbreak, SARS-CoV,
234 demonstrated that ACE2 is found abundantly in the endosomal compartment, specifically co-
235 localizing with the early endosomal marker EEA1 (31). Further, at 3 hpi, SARS-CoV antigens
236 colocalize with vesicular ACE2 and that ACE2 formed notable vesicular puncta in the infected
237 cells (31). We utilized Stimulated Emission Depletion (STED) microscopy, leveraging the super
238 resolution capabilities of this platform to investigate ACE2 and AXL colocalization in uninfected
239 and infected Vero E6 cells. In uninfected cells, AXL and ACE2 were found on the plasma
240 membrane and intracellularly, but colocalize poorly (**Fig. 4G and H**). However, as shown in the
241 micrographs (white arrows) and the associated fluorescence intensity plot profiles (**S4F** yellow
242 lines highlight selected ROI), ACE2 and AXL demonstrate overlapping localization patterns
243 within cytoplasmic punctate structures. Pearson's correlation coefficients of infected and
244 uninfected cells calculated for AXL and ACE2 intensity demonstrate a significant increase in
245 colocalization values between this PS receptor and the cognate SARS-CoV-2 receptor in
246 infected cells, relative to mock counterparts. (**Fig. 4H**). These data support the possibility that
247 PS receptors enhance SARS-CoV-2 trafficking into these intracellular puncta where ACE2 is
248 abundant.

249

250 ***AXL promotes SARS-CoV-2 infection in a range of lung cell lines***

251 In addition to ACE2, many lung cell lines express AXL (19, 32) (**S5A**). We evaluated these lines
252 for their ability to support SARS-CoV-2 infection and whether infection was sensitive to
253 bemcentinib inhibition. The panel of lung cells that were selected included A549
254 (adenocarcinoma) stably expressing ACE2, HCC1650 (NSCLC), HCC1944 (squamous), H1819
255 (adenocarcinoma), H2302 (adenocarcinoma) and Calu3 (adenocarcinoma).

256

257 These cells were inoculated with SARS-CoV-2 (MOI = 0.5 unless otherwise noted) in the
258 presence or absence of a serial dilution of the AXL inhibitor, bemcentinib, or the cysteine
259 protease inhibitor, E-64. The cell lines A549^{ACE2}, H1650, HCC1944, H1819, and HCC2302

260 readily supported SARS-CoV-2 infection, and viral loads 24 hpi were decreased in a dose-
261 dependent manner, by bemcentinib and E64 (**Fig. 5A-E**). Infectious SARS-CoV-2 present in
262 HCC2302 cell supernatants at 24 and 48 hpi were also markedly decreased by bemcentinib
263 (**Fig. 5F**), demonstrating that bemcentinib treatment reduced production of new infectious virus
264 in a dose dependent manner. Further, at 1 μ M of bemcentinib, detectable production of any
265 infectious virus was delayed until 48 hours (L.O.D. = 5 TCID₅₀/mL). In H1650 cells, the ability of
266 bemcentinib to inhibit recently emerged SARS-CoV-2 variants of concern (VOC), Alpha
267 (B.1.1.7) and Beta (B.1.351), was evaluated. While the Alpha VOC replicated poorly in these
268 cells, bemcentinib significantly inhibited virus replication of both variants, providing evidence the
269 efficacy of the AXL inhibitor is not influenced by SARS-CoV-2 adaptative changes (**S5B**).
270

271 SARS-CoV-2 infection of TMPRSS2⁺ Calu-3 cells (**S6A**) was not sensitive to bemcentinib or E-
272 64, again providing evidence that, in this cell line, the route of virus entry was dominated by the
273 TMPRSS2-dependent path, bypassing the use of PS receptors and the endosomal
274 compartment (**Fig. 5G**). These findings stand in contrast to SARS-CoV-2 infection of
275 TMPRSS2⁺ H1650 cells that were markedly bemcentinib and E-64 sensitive and were found to
276 be insensitive to camostat inhibition (**Fig. 5B, S5C**). The paradoxical finding that virus entry into
277 H1650 is sensitive to E64 and bemcentinib despite endogenous TMPRSS2 expression indicates
278 that TMPRSS2-dependent pathways are not always the dominating or default route of SARS-
279 CoV-2 entry and suggests that a more complex balance of events controls which pathway is
280 used. Neither the total amount of cell surface expressed ACE2 nor the intracellular versus
281 extracellular ACE2 ratio appears to determine the route of virus uptake (**S5D**).
282

283 RNA sequencing studies confirmed and extended our findings with bemcentinib in A549^{ACE2}
284 cells. At 24 hpi, 20% of the transcripts in A549^{ACE2} cells mapped to the viral genome. Infection in
285 the presence of 1 μ M bemcentinib significantly decreased the number of viral transcripts present
286 (**Fig. 5H**). Further analysis of potential qualitative changes in viral transcripts indicated that
287 transcript numbers across the genome were reduced, rather than a reduction of specific
288 subgenomic transcripts.
289

290 To directly evaluate the importance of AXL during infection of human lung cells, CRISPR-Cas9
291 technology was used to knock out (KO) AXL expression in H1650 and HCC2302 cells. H1650
292 AXL^{neg}, a biologically cloned AXL-null line, was evaluated along with bulk AXL KO populations
293 of H1650 and HCC2302, denoted as AXL^{low}. The AXL^{neg} clone, which expressed undetectable

294 levels of AXL protein (**Fig. 6A**), supported dramatically lower SARS-CoV-2 virus loads at a
295 range of input MOIs (**Fig. 6B**) and became unresponsive to bemcentinib (**Fig. 6C**),
296 demonstrating an important role for AXL in SARS-CoV-2 infection and indicating that
297 bemcentinib specifically targets AXL. Bulk populations of AXL^{low} H1650 and HCC2302 also
298 supported reduced levels of SARS-CoV-2 infection and were poorly responsive to bemcentinib
299 (**S6A-E**). Taken together, the data presented here demonstrate that SARS-CoV-2 utilizes AXL
300 to enhance virion binding and entry in some lung cell lines, and that this mechanism can be
301 effectively disrupted in human lung cells by small molecule inhibitors and genetic ablation of
302 AXL.

303

304 ***AXL facilitates infection of other betacoronaviruses***

305 To assess the role of AXL in the related betacoronavirus, mouse hepatitis virus (MHV strain
306 A59), we investigated the ability of bemcentinib to inhibit infection in C57BL/6J mouse bone
307 marrow derived macrophages (BMDMs) that express AXL (33-35). As MHV uses the mouse
308 receptor CEACAM as its cognate receptor, this model allowed us to examine the role of AXL
309 with a coronavirus that is ACE2-independent (36). Bemcentinib added to BMDM cultures
310 decreased virus load at 24 hours in a dose-dependent and an MOI-dependent manner (**S7A-B**).
311 At higher MOIs the effect of bemcentinib was diminished. Bemcentinib treatment also inhibited
312 MHV infection in peritoneal macrophages, an MHV permissive population phenotypically and
313 functionally distinct from BMDMs (**S7C**). These studies provide evidence that AXL facilitates
314 infection of multiple members of this enveloped virus family, independent of the cognate
315 receptor used by the virus.

316

317

318 **DISCUSSION**

319 Here, we demonstrate that PS receptors, AXL, TIM-1 and TIM-4, synergize with ACE2 to
320 mediate SARS-CoV-2 infection of HEK 293T cells when ACE2, the cognate receptor for the
321 virus, was expressed at low levels. PS receptors enhanced virion binding to cells in a PS-
322 dependent manner. At higher levels of ACE2 expression, a role for the PS receptors was no
323 longer observed. Similar findings were observed for TMPRSS2-facilitated, ACE2-dependent
324 infection, indicating that when ACE2 is expressed on the plasma membrane at high
325 concentrations these host proteins that assist SARS-CoV-2 entry are no longer required.

326

327 A recent study reported that AXL mediates SARS-CoV-2 infection (19). That report suggested
328 that AXL-mediated virus entry is independent of ACE2 and that AXL binds to the N-terminal
329 domain of SARS-CoV-2 spike. Conclusions from our studies indicate that AXL and other PS
330 receptors mediate enhancement of SARS-CoV-2 infection through interactions with virion-
331 associated PS in an ACE2-dependent manner. We report several lines of evidence that are
332 consistent with our contention that the PS receptors interact with virion-associated PS. First, PS
333 liposomes abrogate binding and entry in a dose dependent manner. Second, interfering with
334 PS/PS receptor complexes by mutating the TIM-1 PS binding pocket abrogates SARS-CoV-2
335 infection. These data are consistent with and support the well-established mechanism of PS
336 receptor enhancement of enveloped virus infection (11-13, 37, 38). Third, we directly tested
337 whether AXL binds to purified Spike or NTD by flow cytometry and biolayer interferometry
338 assays and were unable to detect any interaction. Finally, the ability of diverse PS receptors to
339 enhance SARS-CoV-2 infection in HEK 293T cells lend support to the contention that these
340 receptors interact with PS rather than viral spike on the surface of SARS-CoV-2 to mediate
341 productive infection. Thus, we conclude that AXL does not interact with SARS-CoV-2 spike, nor
342 does it mediate virus entry unilaterally. It should be noted that this is the first example of an
343 enveloped virus that utilizes PS receptors in conjunction with low/moderate expression of a high
344 affinity surface receptor.

345
346 A previous study concluded that the related coronavirus, SARS-CoV, was not productively
347 internalized by PS receptors (11). However, with insights from our studies, an alternative
348 explanation is that PS receptor enhancement of coronavirus entry is ACE2-dependent and
349 sufficient quantities of ACE2 on the plasma membrane abrogate a role for PS receptors. Thus,
350 PS receptors only facilitate SARS-CoV-2 entry under conditions where ACE2 is expressed at
351 suboptimal levels, conditions that were likely not evaluated in the cited study but are found on
352 ACE2 expressing cells such as Vero E6 cells and many patient derived lung cell lines. As ACE2
353 expression is low within the lung, such suboptimal conditions may be highly relevant during
354 SARS-CoV-2 infection (39, 40).

355
356 PS receptors have previously been shown to interact with PS on the surface of other enveloped
357 viruses such as filoviruses, alphaviruses and flaviviruses and mediate internalization into
358 endosomes (11, 41). However, PS receptor-dependent entry is a mechanism that is functionally
359 out-competed by high-affinity viral glycoprotein-host receptor interactions, such as that of Lassa
360 virus with α -dystroglycan (16, 20). In the case of Lassa virus entry PS receptors seem to serve

361 as a backup entry mechanism, as these receptors only mediate virus internalization when the
362 high affinity surface receptor, α -dystroglycan, is not expressed.

363

364 Our studies provide evidence that PS receptors enhance SARS-CoV-2 binding to cells and
365 mediate internalization into endosomes where cysteine proteases potentiate spike protein
366 triggering and subsequent fusion events. Consistent with the utilization of this uptake pathway,
367 the cysteine protease inhibitor E-64 effectively blocked ACE2 or ACE2/PS receptor entry in HEK
368 293T cells. This is also supported by our super resolution microscopy observations that AXL
369 and ACE2 colocalize during SARS-CoV-2 infection. However, in HEK 293T, the route of virus
370 entry changes upon expression of TMPRSS2; virion entry is no longer sensitive to E-64. As
371 others have reported, these findings are consistent with TMPRSS2-dependent entry dominating
372 as the route of entry when TMPRSS2 is expressed (24, 42, 43). We also investigated virus
373 infection of a variety of lung lines that endogenously express TMPRSS2, AXL, and ACE2. While
374 findings with Calu-3 cells were similar to that we observed in TMPRSS2-transfected HEK 293T
375 cells, the other TMPRSS2⁺ lung lines, such as H1650 cells, remained sensitive to E-64 and the
376 AXL signaling inhibitor, bemcentinib. Differences in the ability of TMPRSS2 expression to
377 control the route of entry may be due to a fine balance of surface expression of the various
378 receptors and should be explored in more detail.

379

380 Our data indicate that AXL serves as the most important PS receptor for SARS-CoV-2 infection
381 of the TIM and TAM families and our studies with MHV implicated AXL in facilitating infection of
382 additional coronaviruses. While AXL is abundant on lung epithelial cells, it is also present in
383 many organs in the body, with the exclusion of neural tissues (32, 44). Thus, it is likely a role for
384 AXL in SARS-CoV-2 infection is not only relevant to lung cell populations, but ACE2-expressing
385 tissues suspected to be affected by COVID-19 such as the heart and kidneys (45, 46). We
386 surmise that AXL-inhibiting therapeutics could function in tandem with other antivirals, protecting
387 a number of organs from infection. Our data suggest that the efficacy of bemcentinib will persist
388 as the virus evolves, inhibiting the VOCs Alpha and Beta effectively. By targeting host proteins
389 such as AXL we dramatically reduce the potential selection for pathogen mutants that reduce or
390 abolish antiviral activity. Given that currently utilized small molecule therapeutics such as
391 remdesivir targeting viral proteins have shown limited efficacy and the benefits of antibody-rich
392 convalescent plasma is minimal, AXL inhibition by small molecule inhibitors such as
393 bemcentinib offers a novel route of attack to reduce SARS-CoV-2 entry and disease (47, 48).

394

395 The preferential utilization of AXL rather than TIM-1 by SARS-CoV-2 in Vero E6 cells was
396 unexpected. In our previously studies, other enveloped viruses that utilize PS receptors, such as
397 filoviruses, use TIM-1 preferentially when both proteins are expressed (12, 20). Further, a recent
398 study identified that the TIM-1 IgV domain that contains the PS binding pocket serves as an
399 effective inhibitor of enveloped virus infection regardless of the PS receptor utilized for virus
400 uptake (49), consistent with the good affinity the TIM-1 PS binding pocket has for PS (50).
401 Nonetheless, when TIM-1 is not present in cells and AXL is the sole PS receptor expressed,
402 AXL is used by filoviruses and flaviviruses (11, 13, 51-53). The subpar utilization of AXL
403 reported for other viruses may be due to the requirement for the adaptor protein, Gas6, to also
404 be present, expression patterns, or steric factors. As multiple proteins from a variety of different
405 PS receptors families can mediate uptake of apoptotic bodies, it is no surprise that PS receptor
406 interactions with viruses are likewise intricate. Further studies are needed to understand the
407 preferential use of AXL by SARS-CoV-2.

408
409 Bemcentinib, an orally bioavailable small molecule inhibitor of AXL, is currently in Phase II trials
410 for non-small cell lung cancer (NSCLC) and a variety solid and hematological cancers
411 (ClinicalTrials.gov IDs: NCT03184571, NCT03184558). However, multiple screens have
412 identified bemcentinib as inhibitory to SARS-CoV-2 infection, bolstering this mechanism of entry
413 (54, 55). Two phase 2 clinicals trial evaluating efficacy of bemcentinib in hospitalized COVID-19
414 patients are ongoing, with the first recently reporting short-term efficacy results
415 (<https://clinicaltrials.gov/ct2/show/NCT04890509>). In this exploratory, open-label study
416 bemcentinib was added to standard-of care (SoC) therapy to hospitalized patients (56). Though
417 the primary endpoints (time to improvement by 2 points on WHO ordinal scale or time to
418 discharge) showed a marginal benefit of bemcentinib treatment, there was evidence of
419 potentially meaningful clinical benefit in a key secondary endpoint which was avoidance of
420 deterioration. These interim data are promising and support further clinical investigations of this
421 AXL inhibitor for treating SARS-CoV-2.

422
423 The robust body of PS receptor research completed in the last decade and historical patterns of
424 zoonotic events (Ebola virus, Zika virus, coronaviruses) suggest that future emergent viral
425 pathogens are likely to utilize PS receptors to enhance entry and infection. The observations
426 reported here that PS receptors are utilized by a novel pandemic coronavirus support this
427 conclusion. This confluence of information provides insights into a new class of potential
428 therapeutics to stem future outbreaks, namely drugs aimed at inhibiting PS receptor activity.

429 Further studies are required to determine the role of TIM and TAM use *in vivo*; however, our
430 studies demonstrate a role of PS receptors in SARS-CoV-2 infection in relevant cell populations
431 and further extend the importance of PS receptors in enveloped virus entry to coronaviruses.

432

433 **STAR METHODS**

434

435 **RESOURCE AVAILABILITY**

436 Lead contact:

437 Further information and request for resources and reagents should be directed to and will be
438 fulfilled by the lead contact Wendy J. Maury (wendy-maury@uiowa.edu).

439

440 Materials availability:

441 This study did not generate new reagents.

442

443 **EXPERIMENTAL MODEL AND SUBJECT DETAILS**

444

445 **Ethics statement:** This study was conducted in strict accordance with the Animal Welfare Act
446 and the recommendations in the Guide for the Care and Use of Laboratory Animals of the
447 National Institutes of Health (University of Iowa (UI) Institutional Assurance Number: #A3021-
448 01). All animal procedures were approved by the UI Institutional Animal Care and Use
449 Committee (IACUC) which oversees the administration of the IACUC protocols and the study
450 was performed in accordance with the IACUC guidelines (Protocol #8011280, Filovirus
451 glycoprotein/cellular protein interactions).

452

453 **Mice**

454 The mice (6-8 weeks old, female) used in these studies were obtained from the Jackson
455 Laboratory (C57BL6/J). The protocol (#8011280) was approved by the Institutional Animal Care
456 and Use Committee at the University of Iowa.

457

458 **Primary Cells and Immortal Cell Lines**

459 Bone marrow derived macrophages (BMDM) were isolated and cultured in RPMI-1640
460 supplemented with 10% Fetal Bovine Serum (FBS), 0.5 µg/mL of penicillin and streptomycin
461 (pen/strep) and 50 ng/mL murine M-CSF. Vero E6 cells (ATCC CRL-1586), Vero TMPRSS2,
462 Vero E6 and HEK 293T (ATCC CRL-11268) were cultured in Dulbecco's modified Eagle's

463 medium (DMEM, GIBCO, Grand Island, NY) supplemented with 5-10% FBS and 1%
464 penicillin/streptomycin (GIBCO). Blasticidin (5 μ g/mL) was added to media supporting Vero E6
465 TMPRSS2 cell growth. A549^{ACE2} cells were generated by transduction of A549 (ATCC CCL-
466 185) with a codon-optimized ACE2 encoding lentivirus and selection with 10 μ g/mL blasticidin.
467 Clonal populations were isolated and ACE2 expression verified by western blot. H1650,
468 HCC2302, HCC1944 and H1819 human lung lines were maintained in RPMI with 5-10% FBS
469 and pen/strep. Cell lines were periodically tested for mycoplasma contamination (E-Myco kit,
470 Bulldog Bio, Portsmouth, NH) and cured of contamination before use (Plasmocin, Invitrogen,
471 San Diego CA). Cell lines were authenticated periodically by ATCC (A549 and HEK 293T) or
472 the lab responsible for their generation (H1650, HCC2302, HCC1944, H1819, and Vero
473 TMPRSS2).

474

475 AXL knockout HCC2302 and H1650 were generated by transduction of parental cells with a
476 Cas9 encoding lentivirus (kind gift of Aloysius Klingelhutz, University of Iowa) and selection in
477 10 μ g/mL blasticidin for 10 days. Then cells were transduced with an Invitrogen LentiArray
478 CRISPR gRNA lentivirus targeting AXL, and subsequently selected in puromycin at 2 μ g/mL for
479 5 days. Cells were then lifted, stained for AXL, and sorted for AXL^{low} cells at the University of
480 Iowa Flow Cytometry Core on a FACSaria Fusion (Becton, Dickinson and Company, Franklin
481 Lakes, New Jersey). Bulk populations of AXL^{low} cells were used for experiments as noted, and
482 Clone #4 was generated by sorting single AXL^{low} cells into a 96 well plate. AXL expression was
483 verified by flow cytometry on a FACSVerse (Becton, Dickinson and Company).

484

485 **Viruses**

486 Studies used the 2019n-CoV/USA-WA-1/2020 strain of SARS-CoV-2 (Accession number:
487 MT985325.1) which was propagated on Vero E6 cells. Briefly, Vero E6 cells were inoculated
488 with an MOI of 0.001 in DMEM supplemented with 2% FCS and pen/strep. Media was removed
489 and refreshed 24 hpi. When cells exhibited severe cytopathic effect, generally 72 hpi, cells were
490 freeze-thawed once, transferred to a conical tube, centrifuged at 1000g for 10 minutes, and
491 supernatants were filtered through a 0.45 μ m filter. Virus was sequenced via Sanger
492 sequencing periodically for furin cleavage site mutations (none were detected) and only low
493 passage stocks were used.

494

495 MHV (A59) stocks were generously provided by Dr. Stanley Perlman. Viral stocks were
496 generated on Vero E6 and the TCID₅₀ was determined on HeLa-mCECAM1 cells by
497 identification of cytopathic effect at 5 days.

498

499 Stocks of recombinant vesicular stomatitis virus that expressed SARS-CoV-2 Spike containing
500 the D614G mutation and nano-luciferase (rVSV/Spike) (kind gift of Dr. Melinda Brindley, Univ.
501 GA) were generated in either Vero E6 or Vero E6 TMPRSS2 cells. Cells were infected with a
502 low MOI (~0.005) of virus and input was removed after ~12 h. Upon evidence of cytopathology,
503 supernatants were collected over a three-day period, filtered through a 0.45 µm filter and frozen
504 at -80°C until purified. Supernatants were thawed and centrifuged overnight at 7000 x g to
505 concentrate the virus. The virus pellet was resuspended in endotoxin-free PBS and layered over
506 a 20% sucrose/PBS cushion. Virus was pelleted through the cushion by centrifugation at
507 28,000 rpm in a SW60Ti rotor (Beckman). The virus pellet was resuspended in PBS and the
508 TCID₅₀ was determined on Vero E6 cells.

509

510 All viral titers were determined by a modified Spearman-Karber method as previously described
511 and reported as infectious units (IU)/mL (57).

512

513 **METHOD DETAILS**

514 **Inhibitors**

515 Bemcentinib (BGB324, R428) was provided by BerGenBio ASA (Bergen, Norway) and
516 dissolved in DMSO for *in-vitro* studies. BMS777607 (Millipore Sigma) was dissolved in DMSO.
517 E-64 (Millipore Sigma) was dissolved in DMSO.

518

519 **RNA isolation and qRT PCR**

520 Total RNA for PCR was extracted from cells or tissue using TRIzol (Invitrogen, Cat# 15596018)
521 according to the manufacturer's protocol. Total isolated RNA (1µg) was reverse transcribed to
522 cDNA using the High-Capacity cDNA Reverse Transcription Kit (Applied Biosystems Cat#
523 4368814). The resulting cDNA was used for amplification of selected genes by real-time
524 quantitative PCR using Power SYBR Green Master Mix (Applied Biosystems, Cat# 4368708).
525 Data were collected on QuantStudio 3 and Ct values determined with the QuantStudio Data
526 Analysis software (Applied Biosystems). Averages from duplicate wells for each gene were
527 used to calculate relative abundance of transcripts relative to housekeeping genes (HPRT,
528 GAPDH, mouse cyclophilin) and presented as 2^{-ΔΔCT}.

529

530 **VSV/Spike pseudovirus production**

531 The production of SARS-CoV-2-Spike vesicular stomatitis virus (VSV/Spike) pseudovirions has
532 been described previously (Hoffmann et al., 2020). Briefly, HEK 293T cells were seeded in 10
533 cm tissue culture plates (CellTreat; Ref# 229692). After 48 hours cells were transiently
534 transfected with a SARS-CoV-2-Spike pCG1 plasmid (a kind gift from Dr. Stefan Pohlman as
535 described in Hoffmann et al., 2020) using a standard polyethyleneimine (PEI) protocol. For this
536 transfection, one tube was prepared with 16 µg of plasmid diluted in 1.5 mL of OPTI-Mem
537 (Gibco; Ref# 31985-070). The second tube was prepared with PEI (1mg/mL) diluted in 1.5 mL
538 of OPTI-Mem at a concentration of 3 µl/1 µg of DNA transfected. The tubes were then
539 combined, vortexed for 10-15 seconds and left to incubate at room temperature for 15 minutes.
540 The mixture was then added dropwise to the HEK 293T cells and returned to incubator
541 overnight. Twenty-four hours after transfection the cells were infected with a stock of replication
542 insufficient VSV virions expressing firefly luciferase that were pseudotyped with Lassa virus
543 glycoprotein on the viral membrane surface. The infection was incubated for ~6 hours at 37°C,
544 was removed from the cells, and fresh media was added. Viral collection took place at 24- and
545 48-hours post-infection. Media supernatants were removed from the flasks, briefly spun down to
546 remove cellular debris (180 x g for 1 minute) and filtered through a 0.45 µm syringe-tip disk
547 PVDF filter (CellTreat; Ref# 229745). Supernatants were then concentrated by a 16-hour
548 centrifugation step at 5380 x g at 4°C. Pseudovirions were purified through a 20% sucrose
549 cushion via ultracentrifugation at 28,000 rpm for two hours at 10°C in a Beckman Coulter
550 SW60Ti rotor. Pseudovirus was then resuspended in 1x PBS and stored at -80°C. Pseudovirus
551 was titered using end point dilution on Vero E6 cells. All infections of cells using SARS-CoV-2-S
552 pseudotyped virions were conducted at a volume of virus that gave a relative light unit (RLU) of
553 roughly 100,000 – 200,000 RLU.

554

555 **HEK 293T transfections and plasmids**

556 All transfections were performed in HEK 293T cells, with a total plasmid concentration of 2 µg.
557 Cells were seeded into 6-well tissue culture plate (Dot Scientific; Ref# 667106) at a density of 5
558 x 10⁵ cells/well. Forty-eight hours after cell seeding, cells were transfected with CMV-driven
559 expression vectors of ACE2, TIM-1, TIM-4, AXL, TYRO3, MerTK and TMPRSS2 (see plasmid
560 details below) with a standard PEI transfection protocol. For this transfection one tube was
561 prepared with plasmid DNA and 150 mM NaCl at a concentration of 25 µl/1 µg of DNA
562 transfected. A second tube was prepared with 150 mM NaCl at a concentration of 25 µl/1 µg of

563 DNA transfection along with PEI (1 mg/mL) at a concentration of 3 μ l/ 1 μ g of DNA transfected.
564 Tubes were combined, vortexed vigorously for 10-15 seconds and incubated at room
565 temperature for 15 minutes. Mixtures were added dropwise to HEK 293T cells. For all
566 experiments using ACE2 50 ng of ACE2 plasmid were transfected, unless otherwise noted. For
567 PS receptors, 1000ng of plasmid was transfected unless otherwise noted. All transfections were
568 brought up to 2 μ g total transfected DNA with a PCD3.1 empty expression vector.
569

570 **ACE2 and PS receptor expression detection via flow cytometry**

571 To detect cell surface expression of ACE and PS receptor on transfected HEK293Ts, WT
572 VeroE6s, and AXL knock down/out H1605 and HCC2302 clones, cells were lifted using 1x
573 Versene (GIBCO; Ref# 15040066) at 37°C for ~15 minutes and placed in 5mL polystyrene
574 round-bottom tubes (Falcon Ref# 352052). Cells were washed once with FACS buffer (1x
575 Sterile PBS, 2% FBS, 0.01% sodium azide). Cells were incubated for 30 minutes on ice with
576 primary antibodies diluted in FACS buffer against ACE or PS receptors. Primary antibodies
577 were diluted to 0.75 μ g/mL in FACS buffer prior to incubation. Specific primary antibodies used
578 as follows: goat anti-ACE2 (R&D AF933), goat anti-AXL (R&D154), goat anti-TIM-1 (R&D 1750),
579 goat anti- Tyro3 (R&D AF859), goat anti-TIM-4 (R&D 2929), goat anti-MerTK (R&D AF891),
580 rabbit anti-TMPRSS2 (Abcam ab92323). Cells were washed once with FACS buffer. Cells were
581 then incubated with secondary antibodies at a 1:1000 dilution in FACS buffer on ice for 30
582 minutes. Secondaries used were donkey anti-goat IgG (H+L) Alexa Fluor 647 (Jackson Immuno
583 Research; Ref# 705-605-003) and donkey anti-rabbit IgG (H+L) Alexa Fluor 647 (Invitrogen;
584 A32733). Flowcytometry was performed on a Becton Dickinson FACS Calibur and analyzed by
585 Flow Jo.
586

587 To examine both the surface and intracellular expression of hACE2 on H1650, Calu3,
588 HCC1944, HCC2302, A549^{ACE2} and Vero E6 cells we performed the following protocol. Briefly,
589 cells were staining with Fixable Viability Dye eFluor 780 (eBiosciences), goat anti-human ACE2
590 (R&D AF933) followed by secondary were donkey anti-goat IgG (H+L) Alexa Fluor 647
591 (Jackson Immuno Research; Ref# 705-605-003) To measure the intracellular expression of
592 hACE2, cells were surface stained with Fixable Viability Dye eFluor 780, fixed (PFA 4%),
593 permeabilized (1X PBS + 0.5%Tween20) and stained intracellularly using goat anti-human
594 ACE2 (R&D AF933) followed by secondary donkey anti-goat labeled with AF647. Unstained
595 cells, cells plus viability dye and cells plus secondary antibody/viability dye were included as a

596 control in every staining. Samples were measured on a FACSverse cytometer (BD Biosciences)
597 and data were analyzed with Flowjo software (BD Biosciences).

598

599 **VSV/SARS-CoV-2-spike pseudovirion studies with inhibitors**

600 Following the transfection of HEK 293T cells, cells were incubated for 24 hours. At that time
601 cells were lifted with 0.25% Trypsin (GIBCO; Ref# 25200-056) and plated at a density of 2×10^4
602 cells/well on opaque, flat-bottomed, 96-well plates (Falcon; Ref# 353296). Each transfection
603 was plated into at least 3 wells to create experimental replicates. Cells were incubated for an
604 additional 24 hours. At that time, cells were infected with VSV-luciferase/SARS-CoV-2 Spike.
605 Cells were incubated for an additional 24 hours. For experiments done with inhibitors, cells were
606 treated with the concentrations of inhibitors noted in the figure panel immediately prior to being
607 infected with pseudotyped virions. After 24 h, virus-containing media was removed and replaced
608 with 35 μ l of 1x Passive lysis buffer (Promega; Ref# E194A). Plates underwent three freeze-
609 thaw cycles consisting of freezing on dry-ice for 15 minutes followed by thawing at 37°C for 15
610 minutes. We followed the protocol for measuring firefly luciferase as reported previously
611 (Johnson et al., 2017). For this method 100 μ l of luciferin buffer (100 μ l of luciferin buffer (15
612 mM MgSO₄, 15mM KPO₄ [pH7.8], 1 mM ATP, and 1mM dithiothreitol) and 50 μ l of 1mM d-
613 luciferin potassium salt (Syd Laboratories; Ref# MB000102-R70170)) were added to each well
614 and luminescence was read via Synergy H1 Hybrid reader (BioTek Instruments). Relative
615 luminescence units were read out. Results analyzed by normalizing values to mock transfection
616 with no protease inhibitors.

617

618 **HEK 293T SARS-CoV-2 infection studies**

619 Following PEI transfection with plasmids as described in the previous section, cells were lifted
620 with 0.25% trypsin and plated into 48-well plates at a density of 6×10^4 (Dot Scientific; Ref#
621 667148). In our BSL3 facility, transfected HEK 293T cells were infected at a MOI = 0.5 with
622 SARS-CoV-2. Cells were incubated at 37°C or 24 hours and then treated with TRIzol RNA
623 isolation reagent and removed from the BSL3 facility. RNA extraction and cDNA generation
624 proceeded as described. qRT-PCR was conducted on the cDNA using SARS-CoV-2-Spike and
625 GAPDH primers. Data analyzed using the $\Delta\Delta Ct$ method as described above.

626

627 **Virion binding assays**

628 For Vero E6 binding studies, cells were grown to confluence in 48 well plates. Media was
629 replaced with DMEM supplemented with 2% FBS and the indicated compounds. Cells were

630 incubated at 10°C (preventing internalization and entry) until equilibrated and SARS-CoV-2 was
631 added at MOI 5. Plates were returned to 10°C for 1 hour. Media was then removed and cells
632 were washed three times with cold DPBS (GIBCO, Cat# 14190144), removing any unbound
633 virus. Then 0.05% Trypsin-EDTA (GIBCO, Cat# 25300054) was added to control wells for 5
634 minutes at 37°C, and washed. After the final wash, all media was removed and replaced with
635 TRIzol (Invitrogen, Cat# NCC1701D). RNA was isolated and analyzed as described. Binding
636 studies in HEK 293T cells were performed using rVSV-SARS-CoV-2 Spike virions (rVSV/Spike)
637 and binding was performed at room temperature in IMMULON 2HB flat bottom plates (Thermo
638 Scientific, Waltham, MA).

639

640 **RNA sequencing and analysis**

641 Following indicated treatments and infections that were performed in triplicate or quadruplicate,
642 Vero E6 and A549^{ACE2} cells in 6 well formats were homogenized using QIAshredder tubes and
643 total RNA isolated using the RNEasy kit with DNase treatment (Qiagen). High quality RNA
644 samples that were verified by a Bioanalyzer (Agilent) was quantified and used as input to
645 generate mRNA-seq libraries for the Illumina platform. Paired-end reads were performed at the
646 Paired-end sequencing reads were subject to alignment to suitable reference genomes: human
647 GRCh38 (GCA_000001405.15 - A549 cells), green monkey (Chlsab1/GCA_000409795.2 - Vero
648 E6 cells) and SARS-CoV-2 (MN985325 - both A549 and Vero E6 cells). Alignments to human
649 and monkey genomes were performed using hisat2 v2.0.5, while to viral genome using bowtie2
650 v2.2.9. Aligned reads were counted using featureCounts from subread package v1.5.2. Counted
651 reads were normalized in R, using DESeq2 v1.30.0 and subjected to statistical analysis. The
652 statistical analysis included computation of median based fold changes, Student t-test p values
653 and false discovery rate (multiple testing correction).

654

655 **Purified spike protein flow cytometry binding studies**

656 The NTD-Fc and RBD-Fc constructs were kindly provided by Tom Gallagher. They contain the
657 Fc region of human IgG1 fused to the N-terminal domain of SARS-CoV-2 Spike (residues 1-
658 309) or the RBD-containing C-terminal domain of the S1 subunit (residues 310-529). We also
659 generated an Fc-Spike construct that contains the Fc region of human IgG1 fused to a
660 cleavage-negative form of the Spike ectodomain (subunits S1 and S2, corresponding to
661 positions 1-1274). To eliminate the polybasic furin cleavage site of Spike, we replaced the Arg-
662 Arg-Ala-Arg motif at positions 682-685 with Ser-Ser-Ala-Ser. All proteins were produced by
663 transient transfection of 293T cells using polyethylenimine. Proteins were harvested in 293S

664 ProCDM and purified using Protein A beads. Eluted products were dialyzed against phosphate
665 buffered saline (pH 7.4). All proteins were analyzed by SDS-PAGE and gels were silver stained
666 to verify the purity of the eluted product.

667

668 We measured the binding efficiency of anti-NTD antibody AM121 (Acro Biosystems) to the
669 Spike-based constructs using an enzyme-linked immunosorbent assay (ELISA), as previously
670 described (58, 59). For this purpose, the NTD-Fc, RBD-Fc or Spike-Fc suspended in PBS were
671 attached to 96-well protein-binding plates by incubation at isomolar concentrations (2, 1.37 and
672 5 µg/mL of the probes, respectively). The next day, wells were washed once with buffer
673 containing 140 mM NaCl, 1.8 mM CaCl₂, 1 mM MgCl₂, 25 mM Tris pH 7.5, 20 mg/mL BSA and
674 1.1% low-fat milk. The anti-NTD antibody suspended in the same buffer was then added to the
675 wells at 0.5 µg/mL. Binding of the anti-NTD antibody was detected using a goat anti-human
676 kappa light chain conjugated to horseradish peroxidase (HPR) (BioRad). To normalize for the
677 amount of the bound probes, we also quantified the amount of probe bound to the wells by
678 incubation with an HRP-conjugated goat anti-human antibody preparation. Binding of the HRP-
679 conjugated antibodies was measured by luminescence using SuperSignal West Pico enhanced
680 chemiluminescence reagents and a Synergy H1 microplate reader, as previously described
681 (60).

682

683 To determine binding of the above probes to AXL, we used flow cytometry. Briefly, HEK 293T
684 cells were seeded in 6-well plates (8.5E5 cells per well) and transfected the next day with 1.5 µg
685 of empty vector or plasmids that express AXL or the full-length form of human angiotensin
686 converting enzyme 2 (ACE2) using JetPrime transfection reagent (PolyPlus). Three days after
687 transfection, cells were detached using PBS supplemented with 7.5 mM EDTA and washed
688 once with washing buffer (PBS supplemented with 5% newborn calf serum). Cells were then
689 incubated with the NTD-Fc, RBD-Fc or Spike-Fc probes (at 5 µg/mL) or anti-AXL antibody (at
690 0.75 µg/mL) in the same buffer for one hour on ice and were washed four times with washing
691 buffer. To detect binding of the Fc probes, we used a goat anti-human polyclonal antibody
692 preparation conjugated to Alexa 647. To detect binding of the anti-AXL antibody, we used a
693 goat anti-donkey polyclonal antibody preparation conjugated to Alexa 594. Secondary
694 antibodies were added at a 1:500 dilution and incubated with the cells on ice for one hour. Cells
695 were then washed and analyzed by flow cytometry. Staining was evaluated on a Becton
696 Dickinson FACS Calibur and analyzed by Flow Jo.

697

698 **Biolayer Interferometry**

699 Biolayer interferometry was performed on an OctetRed96 (Pall Forte-Bio, USA) using NiNTA-
700 (Forte-Bio 185101) or Streptavidin- (Forte-Bio 18-5019) coated Dip and Read biosensors for
701 immobilisation of His-tagged or biotin-tagged proteins respectively. All samples were diluted in
702 Kinetic Buffer (0.1% BSA, 0.02% Tween 20, 0.05% Sodium azide in PBS). Biosensors were
703 equilibrated in Kinetic Buffer, and protein (His-tagged SARS-CoV-2 S1 protein NTD, Acro
704 Biosystems, S1D-C52H6; irrelevant control His-tagged β 4 integrin fibronectin type III domain,
705 generous gift from Petri Kursala laboratory; biotinylated tilvestamab anti-AXL antibody,
706 BerGenBio, Norway) at a concentration of 0.7 μ M was loaded for 10 minutes. A baseline was
707 taken for 2 minutes in Kinetic Buffer before testing association of the target binding protein for
708 10 minutes (AXL extracellular domain fused to human IgG Fc region, BerGenBio ASA, 2 μ M;
709 positive control Anti-SARS-CoV2 spike NTD Neutralizing antibody, Acro Biosystems, AM121,
710 0.1 μ M; IgG1 isotype control antibody, BioXcell, BE0297, 0.1 μ M). Results were analyzed in
711 Prism 9.1.1 for MacOS (GraphPad Software, USA) by aligning to the baseline values
712 immediately prior to association and subtracting signal from isotype control.

713

714 **STED sample preparation and image acquisition**

715 12mm #1.5 coverslips (Fisher Scientific; Ref# 12-545-81P) were coated with 0.1% bovine
716 Achilles' tendon collagen diluted in 1x sterile PBS. Collaged solution was incubated at 37 $^{\circ}$ C for
717 2 hours before being plated to 12mm coverslips. Collagen was allowed to incubate on
718 coverslips 12 hours at 37 $^{\circ}$ C. Slips were then rinsed with 1x PBS and dried in 37 $^{\circ}$ C incubator.
719 Slips were stored in sterile 1x PBS until use.

720

721 Vero E6 cells were plated onto collaged coated slips at 30,000 cells/slip. 24 hours after plating,
722 cells were either left uninfected, or infected with SARS-CoV02 (WA-1) at an MOI = 0.01 and
723 incubated for 24 hours. At that time cells were washed once with sterile 1x PBS and then fixed
724 with 4% PFA solution (Electron Microscopy Sciences; Ref# 15710) for 10 minutes at room
725 temperature. Following PFA fixation, cells were washed three times with 1x PBS and stored at
726 4 $^{\circ}$ C until use.

727

728 For immunofluorescent staining, coverslips were incubated for 2 hours at RT with a blocking
729 buffer consisting of 1% Triton X-100, 0.5% sodium deoxycholate, 1% egg albumin and 0.01%
730 sodium azide all suspended in 1x PBS. After 2-hour blockade, coverslips were incubated
731 overnight at 4 $^{\circ}$ C with primary antibodies against hACE2 (goat anti-hACE2; R&D AF933), and

732 hAXL (rabbit anti-hAXL; Cell Signaling C89E7). Cells were washed three times with 1x PBS for
733 5 minutes each. Samples with goat anti-hACE2 primary antibodies were first incubated with
734 donkey anti-goat IgG (H+L) Alexa Fluor 568 (Invitrogen; A-11057) for 1 hour at RT. Cells were
735 washed three times with 1x PBS for 5 minutes. Coverslips incubated with donkey anti-goat
736 Alexa Fluor 568 were then incubated with 5% NGS (Sigma; G9023) for one hour at RT. Cells
737 were washed three times 1x PBS then incubated for one-hour room temperature with goat anti-
738 rabbit IgG (H+L) Alexa Fluor Plus 488 (Invitrogen; A32731TR). After washing three times for 5
739 minutes with 1x PBS cells were fixed to glass microscopy slides (Fisher Scientific; 12-550-15)
740 with 12ul of Prolong Glass mounting medium (Invitrogen; P36982). Coverslips cured for 48
741 hours before imaging.

742
743 Image acquisition was performed on the Leica SP8 3X STED confocal microscope equipped
744 with an HC PL APO C32 100X/1.4 oil objective lens, and LAS X software (Leica Microsystems;
745 version 3.5.5.19976) in the Central Microscopy Research Facility at the University of Iowa.
746 Excitation was performed using a white light laser set to 20% intensity. Depletion was performed
747 with a 660nm laser set at 7% intensity for Alexa Fluor 488, and 775 nm with 16.5% laser for
748 Alexa Fluor 568 fluorophore. Depletion lasers were aligned using the auto STED alignment tool
749 in the LAS X software. Laser strength and gain were adjusted to prevent pixel saturation.
750 Images collected with two-line averages and 2 frame accumulations. Post image analyses
751 include deconvolution using Huygens Professional Software and the deconvolution Wizard auto
752 functionality (Scientific Volume Imaging). Fluorescence intensity plot profiles were created using
753 ColorProfiler plug-in for ImageJ (Dimiter Prodanov). Pearson's correlation coefficients were
754 performed by using freehand ROI selection tool in ImageJ to outline individual cells and
755 performing colocalization calculations using the Colocalization Test plugin (Tony Collins et al.).
756 Depicted are the R values for 20 cells across five separate fields imaged from one coverslip.
757

758 QUANTIFICATION AND STATISTICAL ANALYSIS

759 Statistical analysis was completed in GraphPad Prism v9.0.2 (GraphPad Software, San Diego,
760 CA). Quantification of flow cytometry data was completed in FlowJo v10.7.1 (Becton, Dickinson
761 & Company, Ashland, OR). Statistical significance was defined as $p < 0.05$, and denoted by a
762 single asterisk (*). Details regarding statistical tests used and exact values of n can be found in
763 the corresponding figure legends. All data presented is representative of $n = 3$ independent
764 experiments unless otherwise noted.

765

766 **AUTHOR CONTRIBUTIONS**

767 See Supplemental Figure 8 for author contributions matrix.

768

769 **ACKNOWLEDGEMENTS**

770 This study was primarily supported by NIH/NIAID grant R01 AI134733 (WJM), NIH/NCI grants
771 P50 CA070907 (JM), U54 CA260560 (JM) and a contract from BerGenBio to WJM. DB was
772 supported by NIH grant T32AI007511 (Training in Mechanisms of Parasitism). HVE was
773 supported by T32 GM007337.

774

775 Kaitlyn Bohan graciously designed and created our graphical abstract image. The Cas9/BlastR
776 lentiviral expression vector was generously provided by Aloysius Klingelhutz, PhD. The
777 A549^{ACE2} cell line was kindly provided by Balaji Manicassamy, PhD. Paige Richards assisted
778 isolation of the H1650 AXL^{neg} clone.

779

780 Declaration of Interests: G.G., D.M., and E.C. are employees of BerGenBio ASA, a company
781 with financial interests in this field. Partial funding was provided by BerGenBio ASA. No other
782 authors have competing interests to declare. The funders had no role in study design, data
783 collection, data analysis, decision to publish, or preparation of the manuscript.

784

785 Data presented herein were obtained at the Genomics Division of the Iowa Institute of Human
786 Genetics which is supported, in part, by the University of Iowa Carver College of Medicine. The
787 authors would like to acknowledge vital assistance from Chantal Allamargot, PhD. Imaging was
788 performed using the Leica SP8 STED super resolution confocal available for use in the
789 microscopy core.

790

791 The data presented herein were obtained at the Flow Cytometry Facility, which is a Carver
792 College of Medicine / Holden Comprehensive Cancer Center core research facility at the
793 University of Iowa. The facility is funded through user fees and the generous financial support of
794 the Carver College of Medicine, Holden Comprehensive Cancer Center, and Iowa City
795 Veteran's Administration Medical Center.

796

797 **FIGURE LEGENDS**

798 **Figure 1: PS receptors synergize with ACE2, enhancing SARS-CoV-2 infection of HEK
799 293T cells. A) Cells transfected with expression PS receptor plasmids, AXL or TIM-1, with or**

800 without 50 ng of ACE2 and infected 48 hours later with SARS-CoV-2 (MOI = 0.5). Viral loads
801 were determined 24 hours following infection. **B-C)** PS receptors, TIM-1 (**B**) and AXL (**C**),
802 enhance rVSV-luciferase/Spike infection at low concentrations of ACE2 are transfected. **D)**
803 Virus binding of cells transfected with PS receptor plasmids with or without 50 ng of ACE2.
804 rVSV/Spike was bound to transfected cells at 48 hpi and bound virus was measured via RT-
805 qPCR. **E)** Supernatants from SARS-CoV-2 infected (MOI = 0.5) transfected HEK 293T cells
806 were titered 48 hpi on Vero E6-TMPRSS2 and TCID₅₀ calculated by Spearman-Karber
807 equation. These studies were performed with transfection of 50 ng of ACE2 plasmid. **F)** HEK
808 293T cells transfected with expression PS receptor plasmids, TYRO3 or TIM-4, with or without
809 50 ng of ACE2 and infected 48 hours later with SARS-CoV-2 (MOI = 0.5). Viral loads were
810 determined 24 hours following infection.

811 Data shown are pooled from at least 3 independent experiments (**A, B, C, D, E, F**). Data
812 represented as means \pm SEM. Student's t-test (**A,E**) and multiple t-test (**B,C**), One-Way ANOVA
813 with multiple comparisons (**D&F**); asterisks represent $p < 0.05$.

814 **Figure 2: PS receptors interact with SARS-CoV-2 by binding to PS. A-B)** PS liposomes
815 interfere with rVSV-luciferase/Spike infection. HEK 293T cells transfected with TIM-1 plasmid
816 and 50 ng of ACE2 plasmid (**A**) or AXL plasmid and 50 ng of ACE2 plasmid (**B**) were infected
817 with rVSV-luciferase/Spike in the presence of increasing concentrations of PS or PC liposomes
818 and assessed for luciferase activity at 24 hours following infection. **C)** HEK 293T cells were
819 transfected with WT or PS binding pocket mutant TIM-1 plasmids with or without 50 ng of ACE2
820 expressing plasmid and infected 48 hours later with rVSV-luciferase/Spike pseudovirions.
821 Luminescence fold change were compared to mock transfected lysates that were set to a value
822 of 1. **D)** AXL is unable to directly interact with purified, soluble SARS-CoV-2 spike/Fc. HEK 293T
823 cells transfected with AXL or ACE2 were incubated with soluble spike protein (S1/S2)-Fc, S1
824 RBD-Fc or S1 NTD-Fc and subsequently incubated with an Alexa 647 secondary. Spike protein
825 binding was detected by flow cytometry. **E)** AXL does not bind to the NTD of SARS-CoV-2
826 spike. Biolayer interferometry association curves show that immobilized AXL-Fc fails to interact
827 with purified NTD of spike.

828 Data are pooled from at least 3 independent experiments (**A, B**) or are representative of at least
829 3 experiments (**C, D, E**). Data represented as means \pm SEM. Multiple t-test (**A, B**), One-way
830 ANOVA with multiple comparisons (**C**); asterisks represent $p < 0.05$.

831 **Figure 3: The route of SARS-CoV-2 entry is altered by TMPRSS2 expression. A)** HEK 293T
832 cells were transfected with ACE2 and TMPRSS2 as noted and infected at 48 h with VSV-
833 luciferase/Spike. At 24 hpi, luminescence activity was determined. Findings are shown relative

834 to empty vector (Mock) transfected cells. Panel depicts one representative experiment. Students
835 t-tests. **B)** TMPRSS2 expression enhances rVSV-luciferase/Spike entry at low levels of ACE2
836 expression. HEK 293T cells were transfected as indicated and pseudovirion entry assessed by
837 measuring luminescence activity at 24 hpi. **C)** Transfected HEK 293T cells were transfected and
838 infected with VSV-luciferase/Spike at 48 h in the presence or absence of E-64 (300 μ M).
839 Luciferase activity was determined 24 hpi.

840 Data are pooled from at least 3 independent experiments (**B, C**) or are representative of at least
841 3 experiments (**A**). Data represented as means \pm SEM. Student's T-tests (**A**) Multiple t-tests (**B**),
842 Two-way ANOVA with row-wise multiple comparisons (**C**); asterisks represent $p < 0.05$.

843 **Figure 4: AXL has a prominent role in SARS-CoV-2 entry in Vero E6 cells. A)** PS liposomes
844 interfere with SARS-CoV-2 pseudovirion entry. Vero E6 cells were treated with PS or PC
845 liposomes and incubated with VSV-GFP/Spike pseudovirions for 24 hours. Entry was detected
846 by GFP fluorescence. **B)** PS liposomes disrupt SARS-CoV-2 binding. Vero E6 cells were
847 incubated with SARS-CoV-2 (MOI = 5) at 10°C for 1 hour, washed extensively, and viral load
848 assessed by RT-qPCR. **C)** AXL signaling inhibitor bemcentinib inhibits SARS-CoV-2 infection in
849 Vero E6 cells. Cells were treated with bemcentinib and infected with SARS-CoV-2 (MOI = 0.01).
850 Viral loads were measured 24 hpi by RT-qPCR. **D)** Bemcentinib inhibition of SARS-CoV-2
851 infection is most efficacious at early time points during infection. Vero E6 cells were challenged
852 with SARS-CoV-2 (MOI = 0.01) and treated with either the vehicle control or 1 μ M bemcentinib
853 at the indicated time. Viral loads were measured 24 hpi by RT-qPCR. **E)** Vero E6 cells were
854 treated with 1 μ M bemcentinib, infected with SARS-CoV-2 (MOI = 0.01) and mRNA harvested
855 18 hpi. mRNA was deep sequenced on an Illumina platform, and viral loads were calculated by
856 alignment to the SARS-CoV-2 genome. **F)** Broad spectrum TAM inhibitor BMS-777607 inhibits
857 SARS-CoV-2 infection in Vero E6 cells. Cells were treated with inhibitor at indicated
858 concentrations for 1 hour, challenged (MOI = 0.01), and viral loads measured 24 hpi by RT-
859 qPCR **G)** STED micrographs showing staining for ACE2 (red) and AXL (green) and merged in
860 Vero E6 cells. Insets are enlarged images from regions highlighted by yellow rectangles. White
861 arrows indicate shared vesicular structures between the two channels. Yellow arrowheads
862 indicate objects that are only seen in one channel. Plot profiles are shown in **S4F**, representing
863 signal intensity along the yellow lines in the merged panels. **H)** Pearson's correlation coefficients
864 of ACE2 and AXL were calculated for n=20 mock and infected cells (ROI determined by cell
865 borders).

866 Data are pooled from at least 3 independent experiments (**B, D, F**) or are representative of at
867 least 3 experiments (**A, C, G, H**). Data are represented as means \pm SEM. Multiple t-tests (**A**)
868 student's t-test (**B, C, F, H**); asterisks represent $p < 0.05$.

869 **Figure 5: AXL inhibition reduces SARS-CoV-2 infection in human lung cells. A-F)** SARS-
870 CoV-2 infection is reduced by AXL inhibition in multiple human lung cell lines. In order:

871 A549^{ACE2}, H1650, HCC1944, H1819, HCC2302, Calu3 were treated with the indicated inhibitors
872 for 1 hour and challenged with SARS-CoV-2 (MOI = 0.5) for 24 hours. Viral load was assessed
873 by RT-qPCR. **G)** HCC2302 cells were treated with bemcentinib at the indicated concentrations
874 for 1 hour and infected with SARS-CoV-2 (MOI = 0.5). Input virus was removed 6 hpi and
875 supernatant was collected at 24 and 48 hpi and titered by TCID₅₀ assays on Vero E6-TMPRSS2
876 cells. TCID₅₀/mL was calculated by the Spearmann-Karber method. **H)** A549^{ACE2} were treated
877 with bemcentinib as indicated, infected with SARS-CoV-2 (MOI = 0.5) and mRNA harvested 24
878 hpi. mRNA was sequenced, and viral loads calculated by alignment to the SARS-CoV-2
879 genome.

880 Data are pooled from at least 3 independent experiments (**F**) or are representative of at least 3
881 experiments (**A, B, C, D, E, G**). Data represented as means \pm SEM. Student's t-test; asterisks
882 represent $p < 0.05$.

883 **Figure 6: AXL knockout reduces viral loads and ablates inhibition by bemcentinib. A)**
884 H1650 AXL knockout cells were generated by lentiviral transduction of Cas9 and gRNA
885 targeting AXL, followed by selection, enrichment, and biological cloning. Shown are flow
886 cytometry histograms depicting AXL surface staining (black) and secondary only background
887 (grey), demonstrating loss of AXL expression. **B)** H1650 AXL^{neg} and H1650 Cas9 (parental)
888 lines were challenged with SARS-CoV-2 at indicated MOIs. At 24hpi, viral loads were assessed
889 by RT-qPCR. **C)** H1650 parental and AXL^{neg} lines were treated with indicated concentration of
890 bemcentinib for 1 hour and subsequently challenged with SARS-CoV-2 (MOI = 0.5) and viral
891 loads determine by RT-qPCR 24 hpi.

892 Data are pooled from at least 3 independent experiments (**B, C**) or are representative of at least
893 3 experiments (**A**). Data represented as means \pm SEM. Multiple t-tests; asterisks represent $p <$
894 0.05.

895

896 **SUPPLEMENTAL FIGURE LEGENDS**

897 **Supplemental Figure 1: PS receptors synergize with ACE2, enhancing SARS-CoV-2
898 infection of HEK 293T cells. A)** Representative surface staining of receptors transfected into

899 cells. **B)** Surface expression (MFI) of proteins in mock transfected (empty vector) and
900 transfected HEK 293T at 48 hours after transfection. Background fluorescence is shown for
901 secondary antibodies used in experiment (α -goat or rabbit secondaries). **C)** HEK 293T cells,
902 transfected PS receptors as noted with or without 250 ng of ACE2 were transduced with rVSV-
903 luciferase/Spike. Transduction was assessed 24 hours later via luminescence. **D)** Expression of
904 MerTK did not affect rVSV-luciferase/Spike transduction in the presence of 250 ng of
905 transfected ACE2 plasmid. **E)** Expression of ACE2, TIM-1 or AXL did not enhance infection of
906 VSV-luciferase/Lassa virus GP pseudovirions. HEK 293T cells were transfected with PS
907 receptor plasmids and 50 ng of ACE2 and infected 48 hours later. Panels C-E are shown as fold
908 change of luciferase activity in cell lysates relative to mock transfected lysates that were set to a
909 value of 1.
910 Data shown are pooled from at least three independent experiments (**C**, **D**, and **E**). Data
911 represented as means \pm SEM. One-Way ANOVA with multiple comparisons (**C**, **D**), Student's t-
912 test (**E**); asterisks represent $p < 0.05$.

913 **Supplemental Figure 2: PS receptors interact with SARS-CoV-2 by binding to PS. A)** AXL
914 surface expression in transfected HEK 293T cells. **B)** Soluble purified S1/S2-Fc and NTD-Fc are
915 detected by an NTD monoclonal antibody by ELISA. **C)** All spike-Fc proteins bind and are
916 detected at equivalent levels of ELISA plates.

917 **Supplemental Figure 3: The route of SARS-CoV-2 entry is altered by TMPRSS2**
918 **expression.** ATPLite cytotoxicity assay in H1650 cells, 24 hours following treatment with E64.
919 Data are represented as means \pm SEM.

920 **Supplemental Figure 4: AXL has a prominent role in SARS-CoV-2 entry in Vero E6 cells.**
921 **A)** ACE2, AXL and TIM-1 surface expression MFI in Vero E6 cells, as assessed by flow
922 cytometry. Background fluorescence is shown for secondary antibodies used in experiment. **B)**
923 Cell surface versus intracellular ACE2 expression in VeroE6 cells. Indicated cells were lifted,
924 permeabilized as noted, and stained with anti-ACE2 unconjugated primary antibodies and Alexa
925 647 secondaries. **C)** Bemcentinib toxicity 24 hours after treatment was measured by ATPLite
926 assay in H1650 cell line. **D)** VSV-GFP/Spike entry was measured by flow cytometry 24 hours
927 after challenge to Vero E6 cells treated with bemcentinib. **E)** Vero E6 were treated with ARD5
928 (TIM-1 blocking antibody) 1 hour before infection with rVSV /SARS-CoV-2 Spike or rVSV
929 /EBOV-GP (MOI = 0.01). Viral load was measured 24 hpi by RT-qPCR. **F)** Plot profiles of ACE2
930 and AXL intensity are shown in from STED micrographs in Fig. **4G**, representing signal intensity
931 along the yellow lines in the merged panels.

932 Data in A, C, D and E are shown as means \pm SEM. Multiple t-tests were performed in C and
933 Student's t-test was performed in D and E; asterisks represent $p < 0.05$.

934 **Supplemental Figure 5: AXL inhibition reduces SARS-CoV-2 infection in human lung**
935 **cells. A)** Multiple SARS-CoV-2 permissive cell lines were stained for extracellular ACE2, AXL,
936 TIM-1, and TMPRSS2 protein, and expression was quantified by flow cytometry. Shown are
937 flow cytometry histograms depicting target surface staining (black line) and secondary only
938 background (grey shade) **B)** H1650 cells were treated with 1 μ M of bemcentinib and infected
939 with one of three different variants of SARS-CoV-2: WA-1; B.1.1.7 or B.1.351 (MOI=0.5 for all
940 variants). RNA was isolated at 24 hpi and assessed for virus load. **C)** H1650 cells were infected
941 with SARS-CoV-2 (MOI = 0.5) after treatment with the indicated concentration of camostat for 1
942 hour. Viral loads 24hpi were measured by qRT-PCR. **D)** Extracellular and intracellular staining
943 of ACE2 are shown in multiple cell lines. Presented as frequency positive cells.

944 Data represented as means \pm SEM. Student's t-test; asterisks represent $p < 0.05$.

945 **Supplemental Figure 6: AXL knockout reduces viral loads and ablates inhibition by**
946 **bemcentinib. A)** H1650 and HCC2302 AXL knockout cells were generated by lentiviral
947 transduction of Cas9 and gRNA targeting AXL, followed by selection. These are designated
948 "Bulk AXL^{low}" Shown are flow cytometry histograms depicting AXL surface staining (black) and
949 secondary only background (grey), demonstrating complete loss of AXL expression in H1650
950 AXL^{neg}. **B)** H1650 AXL^{low} and H1650 Cas9 (parental) lines were challenged with SARS-CoV-2 at
951 indicated MOIs for 24 hpi and viral loads assessed by RT-qPCR. **C)** H1650 parental and AXL^{low}
952 lines were treated with indicated concentration of bemcentinib for 1 hour and subsequently
953 challenged with SARS-CoV-2 (MOI = 0.5) and viral loads determine by RT-qPCR 24 hpi. **D-E)**
954 As in B-C with HCC2302 cells.

955 Data are pooled from at least 3 independent experiments (**B, C, D, E**) or are representative of at
956 least 3 experiments (**A**). Data represented as means \pm SEM. Multiple t-tests were performed;
957 asterisks represent $p < 0.05$.

958 **Supplemental Figure 7: A)** Bone marrow derived macrophages from C57bl6/J mice were
959 treated as indicated for 1 hour, challenged with MHV (stain A59) at the indicated MOI. Viral
960 loads were assessed 24 hpi by RT-qPCR. **B)** BMDMs were treated with indicated
961 concentrations of bemcentinib for 1 hour, infected with MHV (MOI = 0.001) for 24 hours and
962 viral load assessed by RT-qPCR. **C)** As in B, MHV infection of peritoneal macrophages (MOI
963 =0.001) treated with indicated concentrations of bemcentinib.

964 Data shown are representative of 3 independent experiments. Data represented as means ±
965 SEM. Student's t-test; asterisks represent p < 0.05.

966

967 **LITERATURE CITED**

- 968 1. Letko M, Marzi A, Munster V. Functional assessment of cell entry and receptor usage for SARS-
969 CoV-2 and other lineage B betacoronaviruses. *Nat Microbiol.* 2020;5(4):562-9.
- 970 2. Wrobel AG, Benton DJ, Xu P, Roustan C, Martin SR, Rosenthal PB, et al. Author Correction:
971 SARS-CoV-2 and bat RaTG13 spike glycoprotein structures inform on virus evolution and furin-cleavage
972 effects. *Nat Struct Mol Biol.* 2020;27(10):1001.
- 973 3. Hoffmann M, Kleine-Weber H, Schroeder S, Krüger N, Herrler T, Erichsen S, et al. SARS-CoV-2
974 Cell Entry Depends on ACE2 and TMPRSS2 and Is Blocked by a Clinically Proven Protease Inhibitor.
975 *Cell.* 2020;181(2):271-80.e8.
- 976 4. Coutard B, Valle C, de Lamballerie X, Canard B, Seidah NG, Decroly E. The spike glycoprotein of
977 the new coronavirus 2019-nCoV contains a furin-like cleavage site absent in CoV of the same clade.
978 *Antiviral Res.* 2020;176:104742.
- 979 5. Hoffmann M, Kleine-Weber H, Pohlmann S. A Multibasic Cleavage Site in the Spike Protein of
980 SARS-CoV-2 Is Essential for Infection of Human Lung Cells. *Molecular Cell.* 2020;78(4):779-+.
- 981 6. Matsuyama S, Nagata N, Shirato K, Kawase M, Takeda M, Taguchi F. Efficient activation of the
982 severe acute respiratory syndrome coronavirus spike protein by the transmembrane protease TMPRSS2.
983 *J Virol.* 2010;84(24):12658-64.
- 984 7. Glowacka I, Bertram S, Muller MA, Allen P, Soilleux E, Pfefferle S, et al. Evidence that TMPRSS2
985 Activates the Severe Acute Respiratory Syndrome Coronavirus Spike Protein for Membrane Fusion and
986 Reduces Viral Control by the Humoral Immune Response. *Journal of Virology.* 2011;85(9):4122-34.
- 987 8. Cantuti-Castelveteri L, Ojha R, Pedro LD, Djannatian M, Franz J, Kuivanan S, et al. Neuropilin-1
988 facilitates SARS-CoV-2 cell entry and infectivity. *Science.* 2020.
- 989 9. Daly JL, Simonetti B, Klein K, Chen KE, Williamson MK, Anton-Plagaro C, et al. Neuropilin-1 is a
990 host factor for SARS-CoV-2 infection. *Science.* 2020.
- 991 10. Kondratowicz AS, Lennemann NJ, Sinn PL, Davey RA, Hunt CL, Moller-Tank S, et al. T-cell
992 immunoglobulin and mucin domain 1 (TIM-1) is a receptor for Zaire Ebolavirus and Lake Victoria
993 Marburgvirus. *Proceedings of the National Academy of Sciences of the United States of America.*
994 2011;108(20):8426-31.
- 995 11. Jemielity S, Wang JJ, Chan YK, Ahmed AA, Li W, Monahan S, et al. TIM-family proteins promote
996 infection of multiple enveloped viruses through virion-associated phosphatidylserine. *PLoS Pathog.*
997 2013;9(3):e1003232.
- 998 12. Moller-Tank S, Kondratowicz AS, Davey RA, Rennert PD, Maury W. Role of the
999 phosphatidylserine receptor TIM-1 in enveloped-virus entry. *J Virol.* 2013;87(15):8327-41.
- 1000 13. Meertens L, Carnec X, Lecoin MP, Ramdasi R, Guivel-Benhassine F, Lew E, et al. The TIM and
1001 TAM Families of Phosphatidylserine Receptors Mediate Dengue Virus Entry. *Cell Host Microbe.*
1002 2012;12(4):544-57.
- 1003 14. Rhein BA, Brouillette RB, Schaack GA, Chiorini JA, Maury W. Characterization of Human and
1004 Murine T-Cell Immunoglobulin Mucin Domain 4 (TIM-4) IgV Domain Residues Critical for Ebola Virus
1005 Entry. *J Virol.* 2016;90(13):6097-111.
- 1006 15. Morizono K, Chen IS. Role of phosphatidylserine receptors in enveloped virus infection. *J Virol.*
1007 2014;88(8):4275-90.
- 1008 16. Fedeli C, Torriani G, Galan-Navarro C, Moraz ML, Moreno H, Gerold G, et al. Axl Can Serve as
1009 Entry Factor for Lassa Virus Depending on the Functional Glycosylation of Dystroglycan. *Journal of*
1010 *Virology.* 2018;92(5).
- 1011 17. Carette JE, Raaben M, Wong AC, Herbert AS, Obernosterer G, Mulherkar N, et al. Ebola virus
1012 entry requires the cholesterol transporter Niemann-Pick C1. *Nature.* 2011;477(7364):340-3.
- 1013 18. Fritz R, Blazevic J, Taucher C, Pangerl K, Heinz FX, Stiasny K. The Unique Transmembrane
1014 Hairpin of Flavivirus Fusion Protein E Is Essential for Membrane Fusion. *Journal of Virology.*
1015 2011;85(9):4377-85.

1016 19. Wang S, Qiu ZY, Hou YN, Deng XY, Xu W, Zheng TT, et al. AXL is a candidate receptor for
1017 SARS-CoV-2 that promotes infection of pulmonary and bronchial epithelial cells. *Cell Research*.
1018 2021;31(2):126-40.

1019 20. Brouillette RB, Phillips EK, Patel R, Mahauad-Fernandez W, Moller-Tank S, Rogers KJ, et al.
1020 TIM-1 Mediates Dystroglycan-Independent Entry of Lassa Virus. *J Virol*. 2018;92(16).

1021 21. Havranek KE, Jimenez AR, Acciani MD, Lay Mendoza MF, Reyes Ballista JM, Diaz DA, et al.
1022 SARS-CoV-2 Spike Alterations Enhance Pseudoparticle Titers and Replication-Competent VSV-SARS-
1023 CoV-2 Virus. *Viruses*. 2020;12(12).

1024 22. Case JB, Rothlauf PW, Chen RE, Kafai NM, Fox JM, Smith BK, et al. Replication-Competent
1025 Vesicular Stomatitis Virus Vaccine Vector Protects against SARS-CoV-2-Mediated Pathogenesis in Mice.
1026 *Cell Host Microbe*. 2020;28(3):465-74 e4.

1027 23. Case JB, Rothlauf PW, Chen RE, Liu ZM, Zhao HY, Kim AS, et al. Neutralizing Antibody and
1028 Soluble ACE2 Inhibition of a Replication-Competent VSV-SARS-CoV-2 and a Clinical Isolate of SARS-
1029 CoV-2. *Cell Host & Microbe*. 2020;28(3):475-+.

1030 24. Hoffmann M, Kleine-Weber H, Schroeder S, Kruger N, Herrler T, Erichsen S, et al. SARS-CoV-2
1031 Cell Entry Depends on ACE2 and TMPRSS2 and Is Blocked by a Clinically Proven Protease Inhibitor.
1032 *Cell*. 2020;181(2):271-80 e8.

1033 25. Kobayashi N, Karisola P, Pena-Cruz V, Dorfman DM, Jinushi M, Umetsu SE, et al. TIM-1 and
1034 TIM-4 glycoproteins bind phosphatidylserine and mediate uptake of apoptotic cells. *Immunity*.
1035 2007;27(6):927-40.

1036 26. Laporte M, Raeymaekers V, Van Berwaer R, Vandeput J, Marchand-Casas I, Thibaut HJ, et al.
1037 The SARS-CoV-2 and other human coronavirus spike proteins are fine-tuned towards temperature and
1038 proteases of the human airways. *PLoS Pathog*. 2021;17(4):e1009500.

1039 27. Ou TL, Mou HH, Zhang LZ, Ojha A, Choe H, Farzan M. Hydroxychloroquine-mediated inhibition
1040 of SARS-CoV-2 entry is attenuated by TMPRSS2. *Plos Pathogens*. 2021;17(1).

1041 28. Yeung ML, Teng JLL, Jia L, Zhang C, Huang C, Cai JP, et al. Soluble ACE2-mediated cell entry
1042 of SARS-CoV-2 via interaction with proteins related to the renin-angiotensin system. *Cell*.
1043 2021;184(8):2212-28 e12.

1044 29. Ravichandran KS. Find-me and eat-me signals in apoptotic cell clearance: progress and
1045 conundrums. *J Exp Med*. 2010;207(9):1807-17.

1046 30. Kondratowicz AS, Lennemann NJ, Sinn PL, Davey RA, Hunt CL, Moller-Tank S, et al. T-cell
1047 immunoglobulin and mucin domain 1 (TIM-1) is a receptor for Zaire Ebolavirus and Lake Victoria
1048 Marburgvirus. *Proc Natl Acad Sci U S A*. 2011;108(20):8426-31.

1049 31. Wang HL, Yang P, Liu KT, Guo F, Zhang YL, Zhang GY, et al. SARS coronavirus entry into host
1050 cells through a novel clathrin- and caveolae-independent endocytic pathway. *Cell Research*.
1051 2008;18(2):290-301.

1052 32. Morales A, Rojo Rello S, Cristobal H, Fiz-Lopez A, Arribas E, Mari M, et al. Growth Arrest-
1053 Specific Factor 6 (GAS6) Is Increased in COVID-19 Patients and Predicts Clinical Outcome.
1054 *Biomedicines*. 2021;9(4).

1055 33. Segawa K, Yanagihashi Y, Yamada K, Suzuki C, Uchiyama Y, Nagata S. Phospholipid flippases
1056 enable precursor B cells to flee engulfment by macrophages. *Proc Natl Acad Sci U S A*.
1057 2018;115(48):12212-7.

1058 34. Subramanian M, Proto JD, Matsushima GK, Tabas I. Deficiency of AXL in Bone Marrow-Derived
1059 Cells Does Not Affect Advanced Atherosclerotic Lesion Progression. *Sci Rep*. 2016;6:39111.

1060 35. Seitz HM, Camenisch TD, Lemke G, Earp HS, Matsushima GK. Macrophages and dendritic cells
1061 use different Axl/Mertk/Tyro3 receptors in clearance of apoptotic cells. *Journal of Immunology*.
1062 2007;178(9):5635-42.

1063 36. Dveksler GS, Pensiero MN, Cardellicchio CB, Williams RK, Jiang GS, Holmes KV, et al. Cloning of
1064 the mouse hepatitis virus (MHV) receptor: expression in human and hamster cell lines confers
1065 susceptibility to MHV. *J Virol*. 1991;65(12):6881-91.

1066 37. Rhein BA, Maury WJ. Ebola Virus Entry into Host Cells: Identifying Therapeutic Strategies.
1067 *Current Clinical Microbiology Reports*. 2015;2(3):115-24.

1068 38. Moller-Tank S, Albritton LM, Rennert PD, Maury W. Characterizing Functional Domains for TIM-
1069 Mediated Enveloped Virus Entry. *J Virol*. 2014;88(12):6702-13.

1070 39. Hou YJ, Okuda K, Edwards CE, Martinez DR, Asakura T, Dinnon KH, 3rd, et al. SARS-CoV-2
1071 Reverse Genetics Reveals a Variable Infection Gradient in the Respiratory Tract. *Cell*. 2020;182(2):429-
1072 46 e14.

1073 40. Sungnak W, Huang N, Becavin C, Berg M, Queen R, Litvinukova M, et al. SARS-CoV-2 entry
1074 factors are highly expressed in nasal epithelial cells together with innate immune genes. *Nat Med*.
1075 2020;26(5):681-7.

1076 41. Moller-Tank S, Maury W. Phosphatidylserine receptors: enhancers of enveloped virus entry and
1077 infection. *Virology*. 2014;468-470:565-80.

1078 42. Shang J, Wan Y, Luo C, Ye G, Geng Q, Auerbach A, et al. Cell entry mechanisms of SARS-CoV-
1079 2. *Proc Natl Acad Sci U S A*. 2020;117(21):11727-34.

1080 43. Shirato K, Kawase M, Matsuyama S. Wild-type human coronaviruses prefer cell-surface
1081 TMPRSS2 to endosomal cathepsins for cell entry. *Virology*. 2018;517:9-15.

1082 44. Uhlen M, Fagerberg L, Hallstrom BM, Lindskog C, Oksvold P, Mardinoglu A, et al. Proteomics.
1083 Tissue-based map of the human proteome. *Science*. 2015;347(6220):1260419.

1084 45. Liu H, Gai S, Wang X, Zeng J, Sun C, Zhao Y, et al. Single-cell analysis of SARS-CoV-2 receptor
1085 ACE2 and spike protein priming expression of proteases in the human heart. *Cardiovasc Res*.
1086 2020;116(10):1733-41.

1087 46. Puelles VG, Lutgehetmann M, Lindenmeyer MT, Sperhake JP, Wong MN, Allweiss L, et al.
1088 Multiorgan and Renal Tropism of SARS-CoV-2. *N Engl J Med*. 2020;383(6):590-2.

1089 47. Simonovich VA, Burgos Pratz LD, Scibona P, Beruto MV, Vallone MG, Vazquez C, et al. A
1090 Randomized Trial of Convalescent Plasma in Covid-19 Severe Pneumonia. *N Engl J Med*.
1091 2021;384(7):619-29.

1092 48. Beigel JH, Tomashek KM, Dodd LE, Mehta AK, Zingman BS, Kalil AC, et al. Remdesivir for the
1093 Treatment of Covid-19 - Final Report. *N Engl J Med*. 2020;383(19):1813-26.

1094 49. Song D-H, Garcia G, Situ K, Chua BA, Hong MLO, Do EA, et al. Development of a blocker of the
1095 universal phosphatidylserine- and phosphatidylethanolamine-dependent viral entry pathways. *Virology*.
1096 2021;560:17-33.

1097 50. Dragovich MA, Fortoul N, Jagota A, Zhang W, Schutt K, Xu Y, et al. Biomechanical
1098 characterization of TIM protein-mediated Ebola virus-host cell adhesion. *Scientific reports*. 2019;9(1):267.

1099 51. Brindley MA, Hunt CL, Kondratowicz AS, Bowman J, Sinn PL, McCray PB, Jr., et al. Tyrosine
1100 kinase receptor Axl enhances entry of Zaire ebolavirus without direct interactions with the viral
1101 glycoprotein. *Virology*. 2011;415(2):83-94.

1102 52. Zhang L, Richard AS, Jackson CB, Ojha A, Choe H. Phosphatidylethanolamine and
1103 Phosphatidylserine Synergize To Enhance GAS6/AXL-Mediated Virus Infection and Efferocytosis. *J Virol*.
1104 2020;95(2).

1105 53. Richard AS, Shim BS, Kwon YC, Zhang R, Otsuka Y, Schmitt K, et al. AXL-dependent infection of
1106 human fetal endothelial cells distinguishes Zika virus from other pathogenic flaviviruses. *Proc Natl Acad
1107 Sci U S A*. 2017;114(8):2024-9.

1108 54. Dittmar M, Lee JS, Whig K, Segrist E, Li M, Kamalia B, et al. Drug repurposing screens reveal
1109 cell-type-specific entry pathways and FDA-approved drugs active against SARS-CoV-2. *Cell Rep*.
1110 2021;35(1):108959.

1111 55. Bouhaddou M, Memon D, Meyer B, White KM, Rezeli VV, Correa Marrero M, et al. The Global
1112 Phosphorylation Landscape of SARS-CoV-2 Infection. *Cell*. 2020;182(3):685-712 e19.

1113 56. Godfrey R. BERGENBIO ANNOUNCES UPDATE FROM INVESTIGATIONAL PHASE II TRIALS
1114 ASSESSING BEMCENTINIB IN HOSPITALISED COVID-19 PATIENTS bergenbio.com2021 [updated
1115 April 19, 2021; cited 2021. Available from: <https://www.bergenbio.com/bergenbio-announces-update-from-investigational-phase-ii-trials-assessing-bemcentinib-in-hospitalised-covid-19-patients/>.

1116 57. Ramakrishnan MA. Determination of 50% endpoint titer using a simple formula. *World J Virol*.
1117 2016;5(2):85-6.

1118 58. Johnson J, Flores MG, Rosa J, Han CZ, Salvi AM, DeMali KA, et al. The High Content of
1119 Fructose in Human Semen Competitively Inhibits Broad and Potent Antivirals That Target High-Mannose
1120 Glycans. *Journal of Virology*. 2020;94(9).

1121 59. DeLeon O, Hodis H, O'Malley Y, Johnson J, Salimi H, Zhai Y, et al. Accurate predictions of
1122 population-level changes in sequence and structural properties of HIV-1 Env using a volatility-controlled
1123 diffusion model. *PLoS Biol*. 2017;15(4):e2001549.

1124

1125 60. Salimi H, Johnson J, Flores MG, Zhang MS, O'Malley Y, Houtman JC, et al. The lipid membrane
1126 of HIV-1 stabilizes the viral envelope glycoproteins and modulates their sensitivity to antibody
1127 neutralization. *Journal of Biological Chemistry*. 2020;295(2):348-62.
1128

Figure 1: PS receptors synergize with ACE2, enhancing SARS-CoV-2 infection.

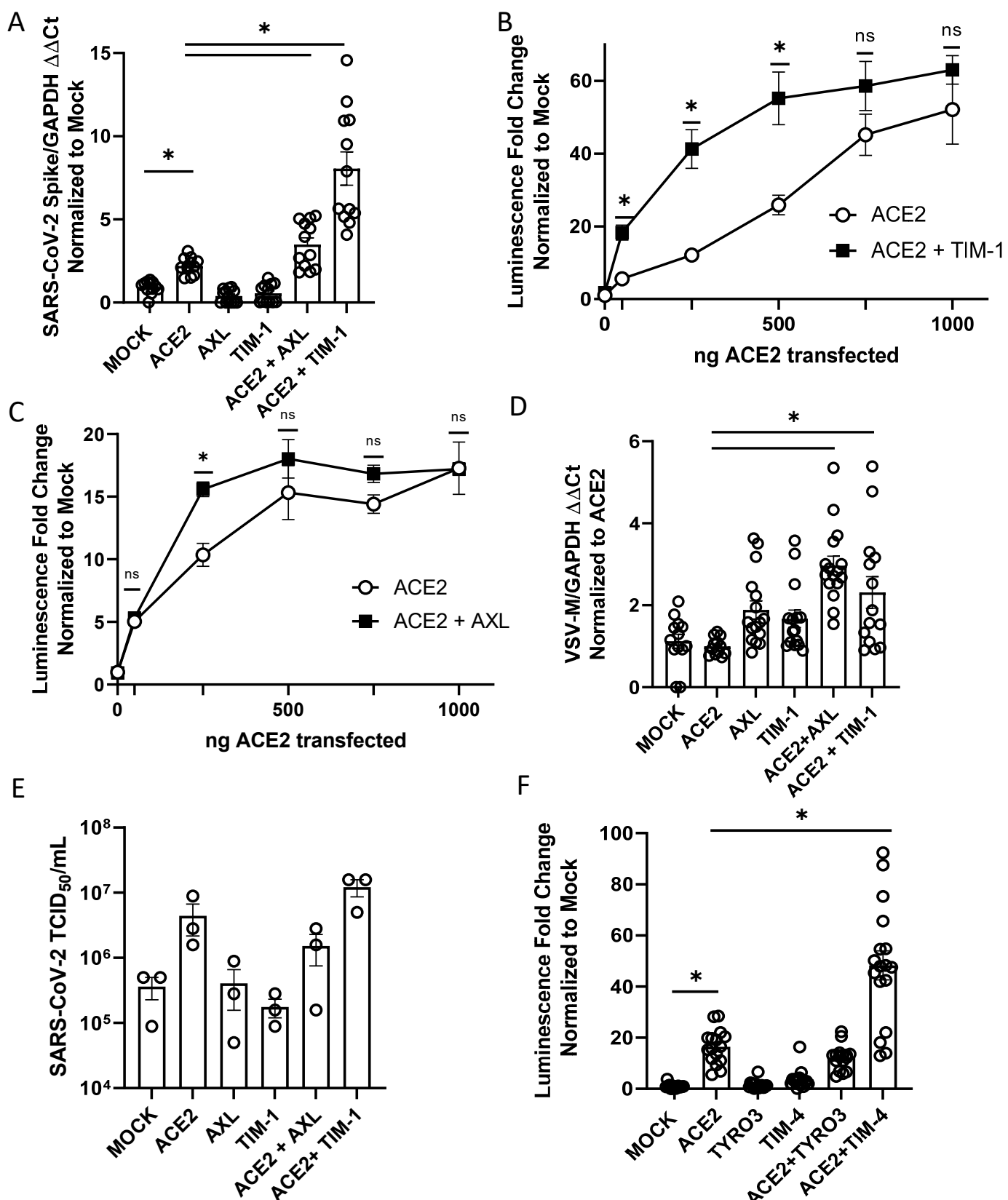


Figure 1: PS receptors synergize with ACE2, enhancing SARS-CoV-2 infection of HEK 293T cells.

A) Cells transfected with expression PS receptor plasmids, AXL or TIM-1, with or without 50 ng of ACE2 and infected 48 hours later with SARS-CoV-2 (MOI = 0.5). Viral loads were determined 24 hours following infection. **B-C)** PS receptors, TIM-1 (**B**) and AXL (**C**), enhance rVSV-luciferase/Spike infection at low concentrations of ACE2 are transfected. **D)** Virus binding of cells transfected with PS receptor plasmids with or without 50 ng of ACE2. rVSV/Spike was bound to transfected cells at 48 hpi and bound virus was measured via RT-qPCR. **E)** Supernatants from SARS-CoV-2 infected (MOI = 0.5) transfected HEK 293T cells were titrated 48 hpi on Vero E6-TMPRSS2 and TCID₅₀ calculated by Spearman-Karber equation. These studies were performed with transfection of 50 ng of ACE2 plasmid. **F)** HEK 293T cells transfected with expression PS receptor plasmids, TYRO3 or TIM-4, with or without 50 ng of ACE2 and infected 48 hours later with SARS-CoV-2 (MOI = 0.5). Viral loads were determined 24 hours following infection.

Data shown are pooled from at least 3 independent experiments (**A, B, C, D, E, F**). Data represented as means \pm SEM. Student's t-test (**A,E**) and multiple t-test (**B,C**), One-Way ANOVA with multiple comparisons (**D&F**); asterisks represent $p < 0.05$.

Figure 2: PS receptors interact with SARS-CoV-2 by binding to PS.

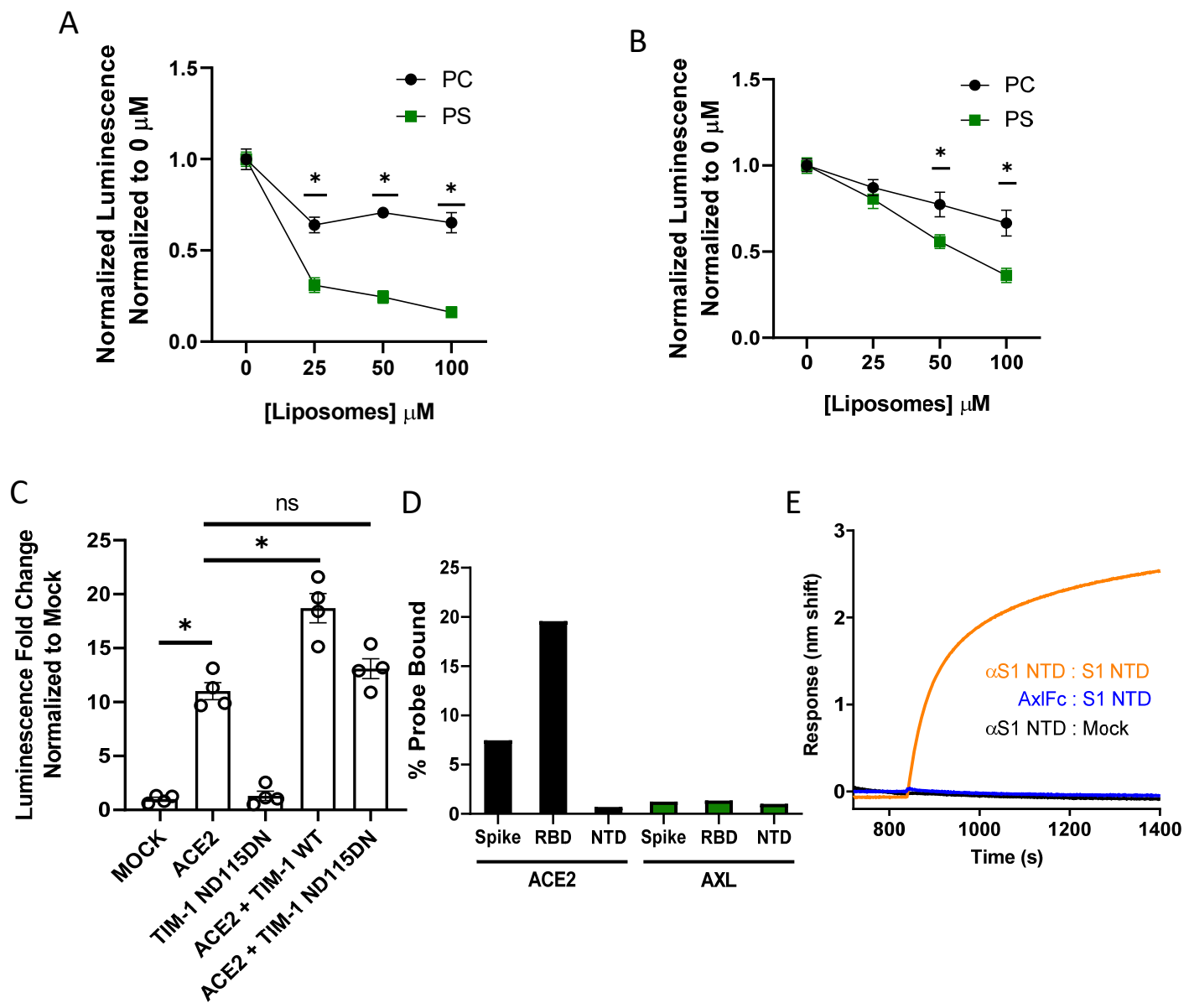


Figure 2: PS receptors interact with SARS-CoV-2 by binding to PS. **A-B)** PS liposomes interfere with rVSV-luciferase/Spike infection. HEK 293T cells transfected with TIM-1 plasmid and 50 ng of ACE2 plasmid (**A**) or AXL plasmid and 50 ng of ACE2 plasmid (**B**) were infected with rVSV-luciferase/Spike in the presence of increasing concentrations of PS or PC liposomes and assessed for luciferase activity at 24 hours following infection. **C)** HEK 293T cells were transfected with WT or PS binding pocket mutant TIM-1 plasmids with or without 50 ng of ACE2 expressing plasmid and infected 48 hours later with rVSV-luciferase/Spike pseudovirions. Luminescence fold change were compared to mock transfected lysates that were set to a value of 1. **D)** AXL is unable to directly interact with purified, soluble SARS-CoV-2 spike/Fc. HEK 293T cells transfected with AXL or ACE2 were incubated with soluble spike protein (S1/S2)-Fc, S1 RBD-Fc or S1 NTD-Fc and subsequently incubated with an Alexa 647 secondary. Spike protein binding was detected by flow cytometry. **E)** AXL does not bind to the NTD of SARS-CoV-2 spike. Biolayer interferometry association curves show that immobilized AXL-Fc fails to interact with purified NTD of spike.

Data are pooled from at least 3 independent experiments (**A, B**) or are representative of at least 3 experiments (**C, D, E**). Data represented as means \pm SEM. Multiple t-test (**A, B**), One-way ANOVA with multiple comparisons (**C**); asterisks represent $p < 0.05$.

Fig. 3. The route of SARS-CoV-2 entry is altered by TMPRSS2 expression

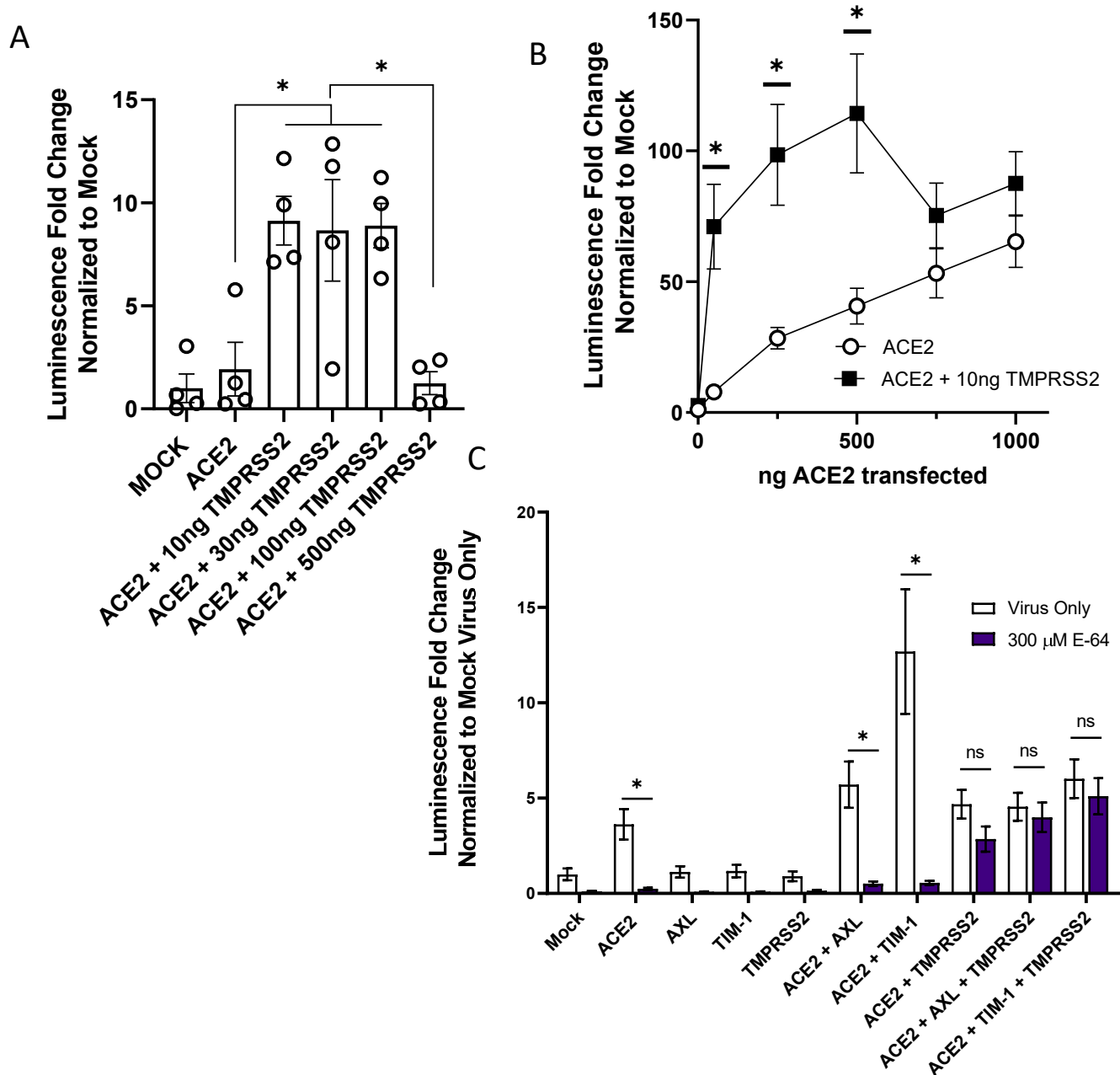


Figure 3: The route of SARS-CoV-2 entry is altered by TMPRSS2 expression. **A)** HEK 293T cells were transfected with ACE2 and TMPRSS2 as noted and infected at 48 h with VSV-luciferase/Spike. At 24 hpi, luminescence activity was determined. Findings are shown relative to empty vector (Mock) transfected cells. Panel depicts one representative experiment. Students t-tests. **B)** TMPRSS2 expression enhances rVSV-luciferase/Spike entry at low levels of ACE2 expression. HEK 293T cells were transfected as indicated and pseudovirion entry assessed by measuring luminescence activity at 24 hpi. **C)** Transfected HEK 293T cells were transfected and infected with VSV-luciferase/Spike at 48 h in the presence or absence of E-64 (300 μ M). Luciferase activity was determined 24 hpi.

Data are pooled from at least 3 independent experiments (**B, C**) or are representative of at least 3 experiments (**A**). Data represented as means \pm SEM. Student's T-tests (**A**) Multiple t-tests (**B**), Two-way ANOVA with row-wise multiple comparisons (**C**); asterisks represent $p < 0.05$.

Figure 4: TAM inhibition reduces SARS-CoV-2 entry, binding, and infection.

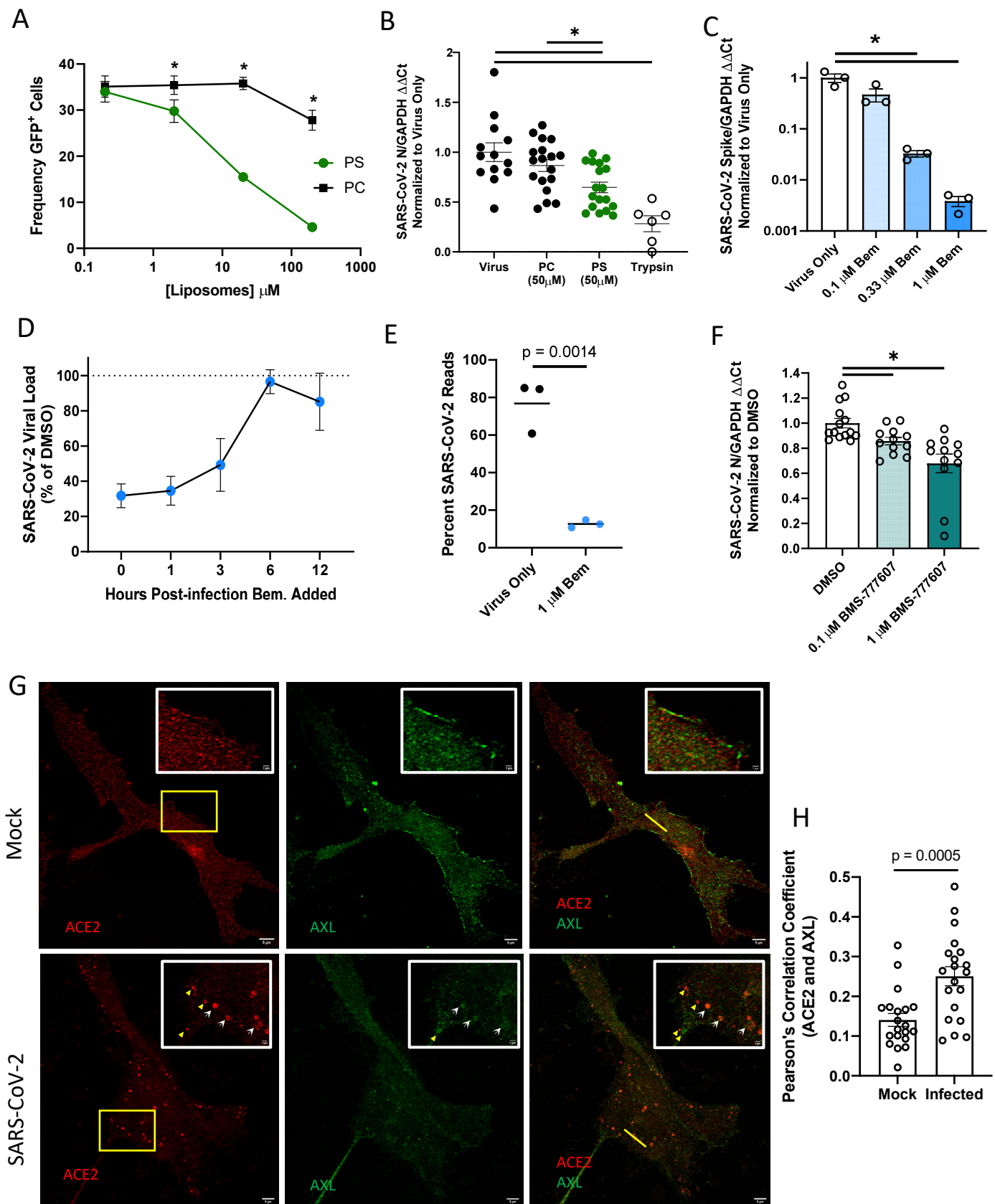


Figure 4: AXL has a prominent role in SARS-CoV-2 entry in Vero E6 cells. **A)** PS liposomes interfere with SARS-CoV-2 pseudovirion entry. Vero E6 cells were treated with PS or PC liposomes and incubated with VSV-GFP/Spike pseudovirions for 24 hours. Entry was detected by GFP fluorescence. **B)** PS liposomes disrupt SARS-CoV-2 binding. Vero E6 cells were incubated with SARS-CoV-2 (MOI = 5) at 10°C for 1 hour, washed extensively, and viral load assessed by RT-qPCR. **C)** AXL signaling inhibitor bemcentinib inhibits SARS-CoV-2 infection in Vero E6 cells. Cells were treated with bemcentinib and infected with SARS-CoV-2 (MOI = 0.01). Viral loads were measured 24 hpi by RT-qPCR. **D)** Bemcentinib inhibition of SARS-CoV-2 infection is most efficacious at early time points during infection. Vero E6 cells were challenged with SARS-CoV-2 (MOI = 0.01) and treated with either the vehicle control or 1 μ M bemcentinib at the indicated time. Viral loads were measured 24 hpi by RT-qPCR. **E)** Vero E6 cells were treated with 1 μ M bemcentinib, infected with SARS-CoV-2 (MOI = 0.01) and mRNA harvested 18 hpi. mRNA was deep sequenced on an Illumina platform, and viral loads were calculated by alignment to the SARS-CoV-2 genome. **F)** Broad spectrum TAM inhibitor BMS-777607 inhibits SARS-CoV-2 infection in Vero E6 cells. Cells were treated with inhibitor at indicated concentrations for 1 hour, challenged (MOI = 0.01), and viral loads measured 24 hpi by RT-qPCR **G)** STED micrographs showing staining for ACE2 (red) and AXL (green) and merged in Vero E6 cells. Insets are enlarged images from regions highlighted by yellow rectangles. White arrows indicate shared vesicular structures between the two channels. Yellow arrowheads indicate objects that are only seen in one channel. Plot profiles are shown in **S4F**, representing signal intensity along the yellow lines in the merged panels. **H)** Pearson's correlation coefficients of ACE2 and AXL were calculated for n=20 mock and infected cells (ROI determined by cell borders).

Data are pooled from at least 3 independent experiments (**B, D, F**) or are representative of at least 3 experiments (**A, C, G, H**). Data are represented as means \pm SEM. Multiple t-tests (**A**) student's t-test (**B, C, F, H**); asterisks represent $p < 0.05$.

Figure 5: AXL inhibition reduces SARS-CoV-2 infection in human lung cell lines

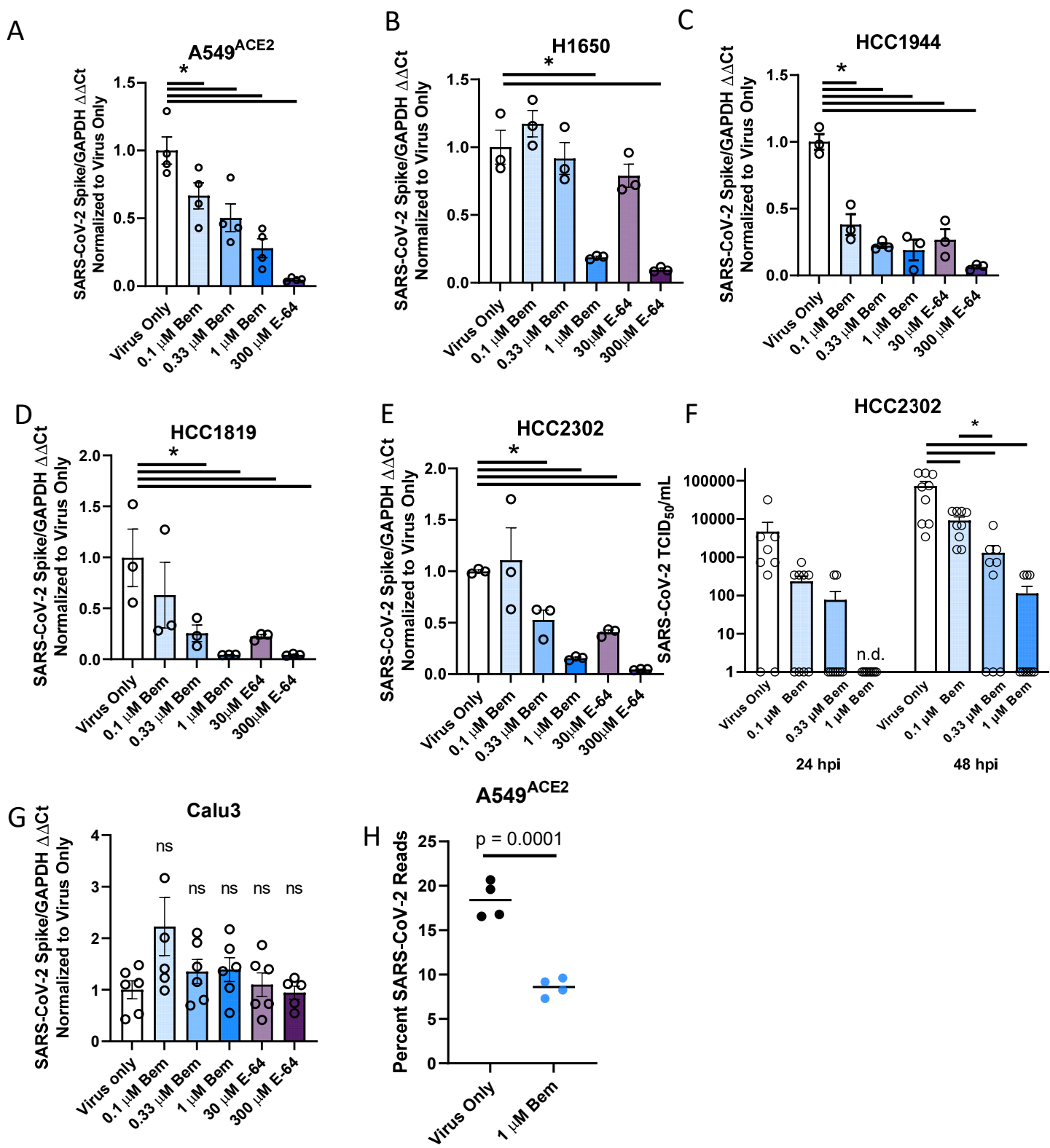


Figure 5: AXL inhibition reduces SARS-CoV-2 infection in human lung cells. A-F) SARS-CoV-2 infection is reduced by AXL inhibition in multiple human lung cell lines. In order: A549^{ACE2}, H1650, HCC1944, H1819, HCC2302, Calu3 were treated with the indicated inhibitors for 1 hour and challenged with SARS-CoV-2 (MOI = 0.5) for 24 hours. Viral load was assessed by RT-qPCR. **G)** HCC2302 cells were treated with bemcentinib at the indicated concentrations for 1 hour and infected with SARS-CoV-2 (MOI = 0.5). Input virus was removed 6 hpi and supernatant was collected at 24 and 48 hpi and titered by TCID₅₀ assays on Vero E6-TMPRSS2 cells. TCID₅₀/mL was calculated by the Spearman-Karber method. **H)** A549^{ACE2} were treated with bemcentinib as indicated, infected with SARS-CoV-2 (MOI = 0.5) and mRNA harvested 24 hpi. mRNA was sequenced, and viral loads calculated by alignment to the SARS-CoV-2 genome.

Data are pooled from at least 3 independent experiments (**F**) or are representative of at least 3 experiments (**A, B, C, D, E, G**). Data represented as means \pm SEM. Student's t-test; asterisks represent $p < 0.05$.

Figure 6: AXL knockout dramatically reduces viral loads and ablates inhibition by bemcentinib.

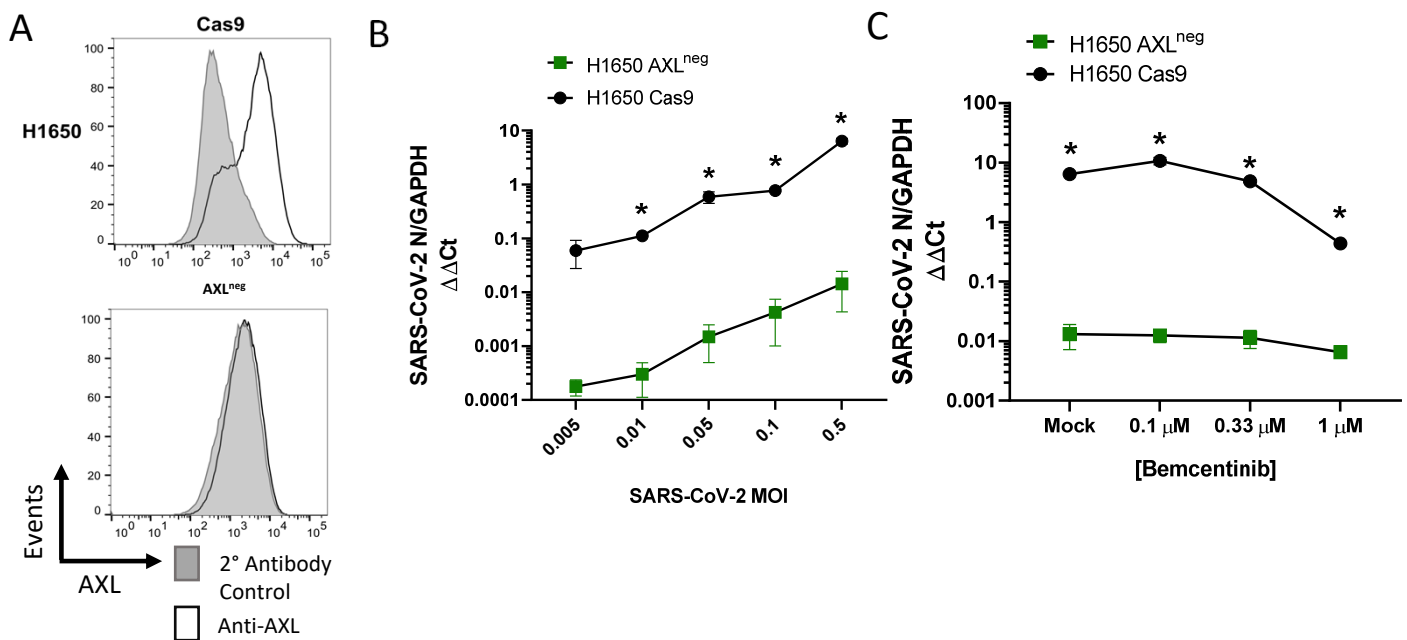


Figure 6: AXL knockout reduces viral loads and ablates inhibition by bemcentinib. A) H1650 AXL knockout cells were generated by lentiviral transduction of Cas9 and gRNA targeting AXL, followed by selection, enrichment, and biological cloning. Shown are flow cytometry histograms depicting AXL surface staining (black) and secondary only background (grey), demonstrating loss of AXL expression. **B)** H1650 AXL^{neg} and H1650 Cas9 (parental) lines were challenged with SARS-CoV-2 at indicated MOIs. At 24hpi, viral loads were assessed by RT-qPCR. **C)** H1650 parental and AXL^{neg} lines were treated with indicated concentration of bemcentinib for 1 hour and subsequently challenged with SARS-CoV-2 (MOI = 0.5) and viral loads determine by RT-qPCR 24 hpi. Data are pooled from at least 3 independent experiments (**B, C**) or are representative of at least 3 experiments (**A**). Data represented as means \pm SEM. Multiple t-tests; asterisks represent $p < 0.05$.